The Astrophysical Journal, 929:50 (17pp), 2022 April 10 https://doi.org/10.3847/1538-4357/ac5c4b

Unveiling an Old Disk around a Massive Young Leaking Blueberry in SDSS-IV MaNGA

Abhishek Paswan[1,2], Kanak Saha[1], Anshuman Borgohain[3], Claus Leitherer[4], and Suraj Dhiwar[1,5]
[1] Inter-University Centre for Astronomy and Astrophysics, Ganeshkhind, Post Bag 4, Pune 411007, India; paswanabhishek@iucaa.in
[2] Indian Institute of Astrophysics, Koramangala Block II, Bangalore 560034, India
[3] Department of Physics, Tezpur University, Napaam 784028, India
[4] Space Telescope Science Institute, Baltimore, MD 21218, USA
[5] Department of physics, Savitribai Phule Pune University, Pune 411007, India
Received 2021 June 2; revised 2022 February 25; accepted 2022 March 7; published 2022 April 12

Abstract

Extreme emission-line galaxies, such as blue compact dwarfs (BCDs), Green Peas (GPs), and blueberries in the local universe are potential candidates for understanding the nature of galaxies that reionized the early universe. Being low-mass, metal-poor starburst systems, they are understood to be local analogs of the high-redshift Lyman continuum and Lyα emitters (LAEs). Even with their proximity to us, we know little about their spatially resolved properties; while most blueberries and GPs are indeed compact, they remain unresolved. Here, we report the detection of a disk-like lower-surface-brightness (LSB) stellar host with a very old population around a blueberry LAE system using broad *i*-band imaging and integral field spectroscopic data from the SDSS and SDSS-IV MaNGA surveys, respectively. The LSB stellar host is structurally similar to that observed around local starburst BCDs. Furthermore, the kinematics of the studied blueberry source bears signs of misalignment between the gas and stellar components. Our findings establish an intriguing thread connecting the blueberry and an LSB disk with an old stellar population and suggest that blueberries and their high-redshift counterparts such as GPs do not represent peculiar cases of dwarf galaxy evolution. In fact, with respect to the structural properties of their host galaxies, they are compatible with a common evolutionary track of the main population of local BCDs.

Unified Astronomy Thesaurus concepts: Compact galaxies (285); Compact dwarf galaxies (281)

1. Introduction

Compact, emission-line, low-mass star-forming (CELLs) galaxies with a high ionization parameter (characterized by large values of [OIII]/[OII] $\gtrsim$ 5) and low oxygen abundance ($7.1 \leqslant 12 + \log(\mathrm{O/H}) \leqslant 8.6 \equiv$ metallicity hereafter) such as Green Peas (GPs; Cardamone et al. 2009) and blueberries (the nearby counterparts of GPs; Yang et al. 2017a) are now believed to be potential sources of escaping Lyman continuum (LyC; Izotov et al. 2016, 2018b) and Lyα (Lyα; Jaskot et al. 2019) photons in the local universe. Their high-redshift analogs are thought to have played a key role in the reionization of our early universe (Shapley et al. 2016; Bian et al. 2017; Vanzella et al. 2018; Fletcher et al. 2019; Saha et al. 2020). Although there has been tremendous progress enhancing our knowledge of these galaxies as LyC and Lyα leakers (Nakajima & Ouchi 2014; Kimm et al. 2017; Trebitsch et al. 2017; Verhamme et al. 2017; Yang et al. 2017b; Izotov et al. 2018a; Wang et al. 2019; Trebitsch et al. 2020), little is known about their whereabouts—especially the morphological structure of their stellar and gas components, composition of the underlying stellar populations, star formation history (SFH), kinematics of stars and gas, and finally their origin.

The extreme emission-line properties, as noticed in the case of GP and blueberry systems, have also been observed in extremely metal-poor blue compact dwarf (XBCD) galaxies (Terlevich et al. 1991; Izotov et al. 1997; Papaderos et al. 1998, 2008), including a few ultracompact dwarf galaxies (e.g., Reverte et al. 2007). The locations of GPs on the fundamental plane (i.e., the mass–metallicity and luminosity–metallicity relations) are found systematically offset to lower metallicities, compared to the majority of local star-forming galaxies (SFGs; Amorín et al. 2010). This implies that GPs and their local counterparts (i.e., blueberries) most likely form a distinct class of objects, along with local XBCDs (Guseva et al. 2009) and a few luminous BCDs at low and intermediate redshifts (Östlin et al. 2001; Hoyos et al. 2005; Kakazu et al. 2007; Salzer et al. 2009) and most SFGs at high redshift (Pettini et al. 2001; Pérez-Montero et al. 2009; Finkelstein et al. 2011). Based on their extreme emission-line properties, Cardamone et al. (2009) and Yang et al. (2017a) suggested that GPs and blueberries could potentially be classified as part of the heterogeneous luminous BCD category. Furthermore, the work by Izotov et al. (2011) also showed that GPs are a subset of luminous compact galaxies whose metallicities are similar to low-luminosity BCDs. However, it remains unclear whether the morphological structure and SFHs of GPs and blueberries are similar to those of luminous BCDs. It is well known that XBCDs and some luminous BCDs possess a compact to moderately extended stellar host underlying their recent star formation component (Papaderos et al. 2008 and references therein). This indicates that these systems have not experienced in situ formation of their first generation of stellar population in a galaxy-wide starburst. In fact, their exponential light profile at the outskirts and the structural properties of their host are found to be fairly comparable to the bona fide old and metal-rich BCDs, containing a low-mass fraction of very old ($\sim$10 Gyr) stars as well (e.g., Kunth et al. 1988; Papaderos et al. 1996a, 1996b; Cairós et al. 2001; Noeske et al. 2003; Guseva et al. 2004; Gil de Paz & Madore 2005; Papaderos et al. 2008). Such morphologies, stellar populations, and SFHs in the case of GPs and blueberries remain less explored. The existence of an old stellar population, in particular in the low-mass end of the galaxy mass spectrum

(i.e., the CELLs galaxies), may shed further light on our current understanding of the formation of disks and stellar feedback (Mo et al. 1998; Ferrara & Tolstoy 2000; Dutton 2009; Sales et al. 2009; Agertz et al. 2011; Übler et al. 2014; Rathaus & Sternberg 2016).

In the recent past, most CELLs galaxies (i.e., GPs and blueberries) have been discovered and studied using data from the Sloan Digital Sky Survey (SDSS; Lintott et al. 2008, 2011), where this survey provides us with seeing-limited (∼1.″2 FWHM) images and fiber-slit (3″ in diameter; York et al. 2000) based spectra with poor signal-to-noise-ratio (S/N) and shallow sensitivity (Abazajian et al. 2009; Blanton et al. 2017). As a result, the CELLs galaxies remain unresolved in the SDSS images, preventing one from further exploring their spatially resolved morphological structure. A similar status prevails on the spectral side. So far, it has not been possible to find direct observational evidence of an old stellar population in these galaxies. At the same time, SDSS spectra do not allow one to spatially resolve the kinematics of stars and gas. A number of efforts have been made to observe these galaxies using the Hubble Space Telescope (HST) Cosmic Origins Spectrograph (COS) in the ultraviolet (UV) domain (e.g., Izotov et al. 2016, 2018a, 2018b; Rong et al. 2018; Malkan & Malkan 2021; Izotov et al. 2021; Kim et al. 2021). These observations have brought us significant information on the UV morphologies that are characterized by bright star-forming knots in the central region of some of these GPs and blueberries. Although these observations (mostly tracing the spatial distribution of young stars) reveal the presence of possible exponential UV disks having scale lengths in the range of 0.6–1.4 kpc, the results are, however, hampered by the limited unvignetted aperture of the HST/COS spectrograph.

In order to overcome issues with spatial resolution and spectroscopic sensitivity to study the morphological structure, stellar population, and SFHs of the GP galaxies, Amorín et al. (2012) presented for the first time three GPs observed with HST *R*-band imaging and long-slit deep optical spectroscopy using the OSIRIS instrument mounted on the 10.4 m GTC. In their spatially resolved images of GPs, they found that these systems seem to have a compact (∼5 kpc) and irregular morphology of their high-surface-brightness components, similar to typical BCDs. Furthermore, they also reported the presence of a lower-surface-brightness (LSB) envelope with an exponentially decreasing intensity at the outskirt, presumably due to an underlying old stellar population. But they could not rule out if this was a generic property of extended nebular halos that are expected to be present in dwarf galaxies with strong starburst events. In one of the GPs, they did provide direct evidence for the old stellar population through the detection of a weak Mg I λ5173 absorption line (GP 113303; Amorín et al. 2012). Overall, their study concludes that GPs are old galaxies with most of the stellar masses formed several gigayears ago. A similar conclusion has also been reached in a recent work by Clarke et al. (2021) with HST imaging of nine GPs in the F555W and F850LP filters. Although stellar kinematics of GPs remain largely unexplored, gas kinematics was presented in four GPs using integral field unit (IFU) spectroscopic observations (Lofthouse et al. 2017). Overall, the underlying physical nature of the CELLs galaxies is still limited and no doubt in need of further exploration with promising IFU observations.

In the current work, we present a CELLs galaxy (viz. SHOC 579 or MaNGA ID: 8626−12704, R.A.: $17^{h}\ 35^{m}\ 01.25^{s}$ and decl.: $+57^{d}\ 03^{m}\ 09^{s}$; see the left panel in Figure 1) observed with optical IFU spectroscopy by the Mapping Nearby Galaxies at Apache Point Observatory (MaNGA; Bundy et al. 2015). SHOC 579 is the only nearby Lyα-emitting galaxy ($z \sim 0.0472$) that is observed in the MaNGA IFU survey. The escape fraction of Lyα photons is measured to be $f_{\mathrm{Ly}\alpha}^{\mathrm{ecp}} \sim 10\%$ (see Jaskot et al. 2019). The close proximity of SHOC 579 in combination with its observed MaNGA IFU data having a better S/N compared to single fiber-slit-based SDSS data provides us a unique opportunity to address the above-mentioned missing properties of blueberry galaxies in unprecedented detail.

Throughout the paper, we have considered a flat ΛCDM cosmology with $H_0 = 70$ km s^{-1} Mpc^{-1}, $\Omega_m = 0.3$, and $\Omega_\Lambda = 0.7$, where H_0 represents the Hubble constant, and Ω_m and Ω_Λ are matter and dark energy density, respectively. All magnitudes quoted in the paper are in the AB system (Oke 1974).

2. Data and Galaxy Selection

The data used in the present study come from the 16th data release (DR16) of the MaNGA survey. This survey is an optical IFU spectroscopy observing program under the fourth generation of SDSS survey (SDSS-IV; Bundy et al. 2015). It uses the BOSS spectrograph (Smee et al. 2013) mounted on the 2.5 m Sloan Foundation Telescope (Gunn et al. 2006) at Apache Point Observatory (APO). Here, the selected IFU sizes are such that it covers at least 1.5 R_e of the observed galaxies (Law et al. 2016). This survey is targeted to observe ∼10,000 nearby ($0.01 < z < 0.15$) galaxies having stellar mass $\geqslant 10^9\ M_\odot$ (Wake et al. 2017). In this survey, the spectra cover a wavelength range of 3600–10300 Å, with a spectral resolution of $R \sim 2000$ and velocity resolution of $\sigma \sim 60$ km s^{-1}. The observed raw IFU datacube is first reduced and calibrated using the Data Reduction Pipeline (DRP; Law et al. 2016) and then analyzed after running the Data Analysis Pipeline (DAP; Westfall et al. 2019) over DRP products. DAP uses the pPXF code (Cappellari & Emsellem 2004) with MILES stellar libraries to fit both the spectra and continuum spectrum simultaneously and provides spectral line fluxes and their equivalent width (EW) maps including gas and stellar kinematics (e.g., v_{stellar}, $\sigma_{\mathrm{stellar}}$, v_{gas}, and σ_{gas}), etc. Note that all the derived 2D maps of various physical parameters have an effective spatial resolution of 2.″5 FWHM. All the emission-line fluxes used in this study are corrected for both Galactic and internal extinctions. First, Galactic reddening is applied by assuming the reddening law provided by O'Donnell (1994). Then, an internal reddening correction to the galaxy is applied using the flux ratio of $f_{\mathrm{H}\alpha}/f_{\mathrm{H}\beta}$ by assuming its theoretical value to be 2.86 and Case B recombination (Osterbrock & Bochkarev 1989) with an electron temperature of $\sim 10^4$ K and electron density of 100 cm^{-3}. For some spaxels, the flux ratio of $f_{\mathrm{H}\alpha}/f_{\mathrm{H}\beta}$ is found to be less than the theoretical value of 2.86. A low value of $f_{\mathrm{H}\alpha}/f_{\mathrm{H}\beta}$ is often associated with intrinsically low reddening (Paswan et al. 2018, 2019), and hence we assumed an internal $E(B-V)$ value of zero for such cases.

Apart from the MaNGA data, other ancillary data are used from several publicly available ground and space-based sky surveys such as GALEX, SDSS, 2MASS, and Spitzer. These data are further analyzed using standard packages available in Python (Van Rossum & Drake 2009), SExtractor (Bertin & Arnouts 1996), GALFIT (Peng et al. 2002), and IRAF (Tody 1986), wherever required.

The galaxy in this study is selected from our search program of blueberry candidates in DR16 of the MaNGA survey. In

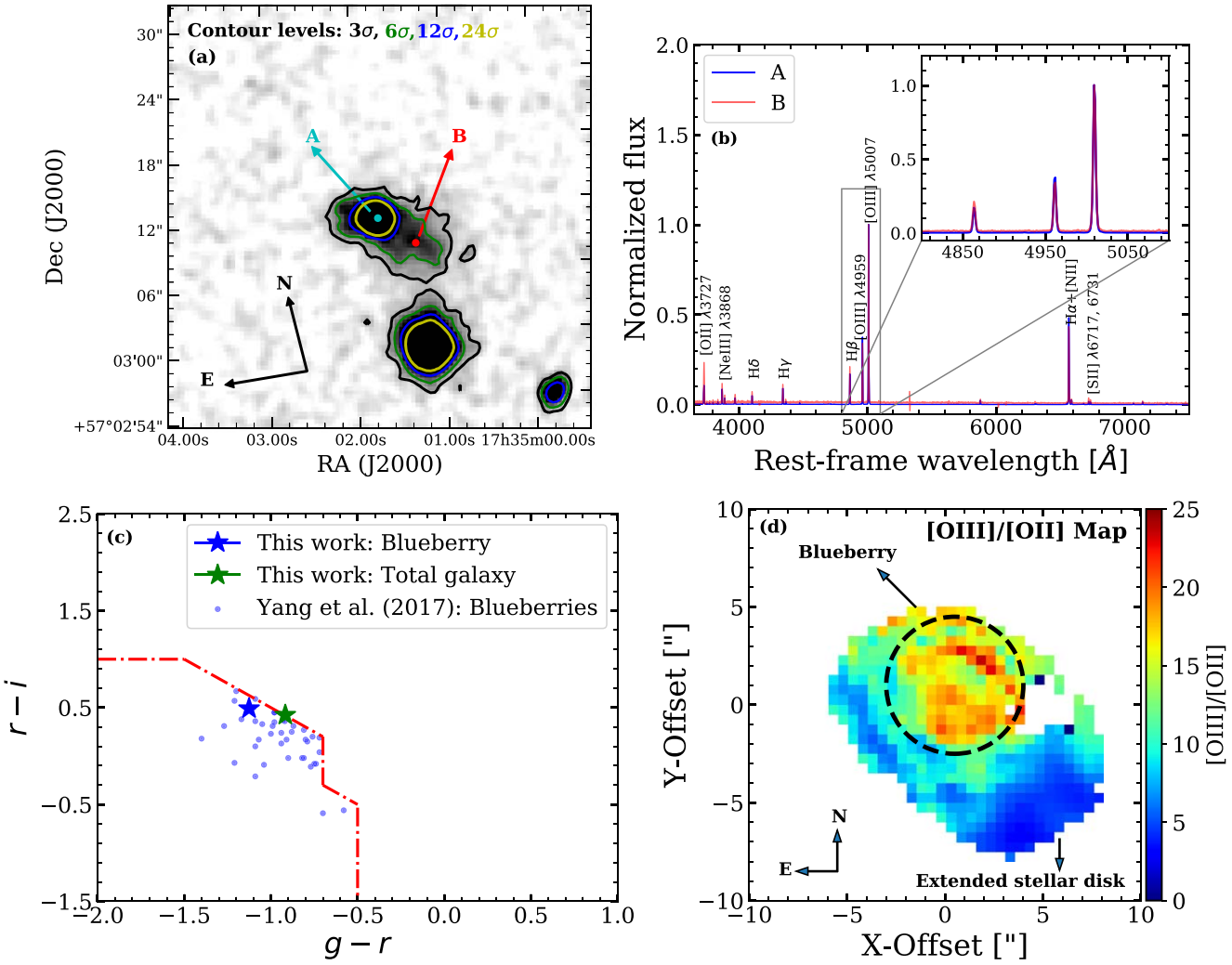

Figure 1. (a) SDSS *i*-band image of the galaxy shown in gray scale overlaid with contours at 3σ, 6σ, 12σ, and 24σ significance levels. The blueberry and extended disk regions are denoted by letters "A" and "B," respectively. (b) One-dimensional spectra extracted from regions "A" and "B," indicating that these two spectra belong to the same system at $z \sim 0.0472$. The identified emission lines are labeled by their respective names. (c) $g - r$ vs. $r - i$ color–color diagram used for classification of the blueberries (Yang et al. 2017a). (d) O_{32} map—the blueberry region is marked by the dashed circle.

order to select the potential candidates, we applied the following criteria to each galaxy in the entire MaNGA sample:

1. $O_{32} \gtrsim 5$
2. EW(Hβ) $\gtrsim$ 100 Å,
3. EW([O III] λ5007) $\gtrsim$ 500 Å.

By applying criterion (1), we found a total of 50 galaxies. Out of these 50, we found only three potential blueberry candidates that satisfied the last two criteria, (2) and (3). Of these three candidates, two are already presented in Paswan et al. (2021). These two blueberries have been found in close association with LSB-disk galaxies, and they are found to be in an advanced state of a merger. The remaining galaxy, known as SHOC 579, is studied here in detail.

3. Basic Properties of the Selected Blueberry Galaxy

In this section, we outline the basic properties of the galaxy SHOC 579. Figure 1(a) displays the SDSS *i*-band image of the galaxy that hosts a bright central compact structure along with surrounding faint disk-like structure within the 3σ outer contour. In order to confirm whether both structures belong to the same system, we extract their corresponding spectra as shown in Figure 1(b). The spatial locations of these spectra are marked by A and B in Figure 1(a). In both cases, using the measurement of the redshift based on the strong emission lines, e.g., Hα and [O III], we confirm that both the compact central structure and the disk-like outer structure are at the same redshift, $z \sim 0.0472$.

Figure 1(c) shows the galaxy SHOC 579 on the SDSS $g - r$ versus $r - i$ color–color diagram. The color cut marked by the red dashed–dotted line has been used to classify a galaxy as a blueberry in the low-redshift ($0.02 \leqslant z \leqslant 0.05$) universe (Yang et al. 2017a). Although the full galaxy lies at the color-cut boundary, the central bright region qualifies as a blueberry on par with other confirmed blueberries identified by Yang et al. (2017a). The colors for the central bright region and total galaxy are separately estimated (see Appendix A for details). Although our selected galaxy was observed earlier in the DR7 of the SDSS survey, it was missed in the previous blueberry sample presented by Yang et al. (2017a), most likely due to their selected flag criteria. In their sample, they flagged those galaxies represented by "CHILD" in the SDSS survey. Similar to the typical properties of

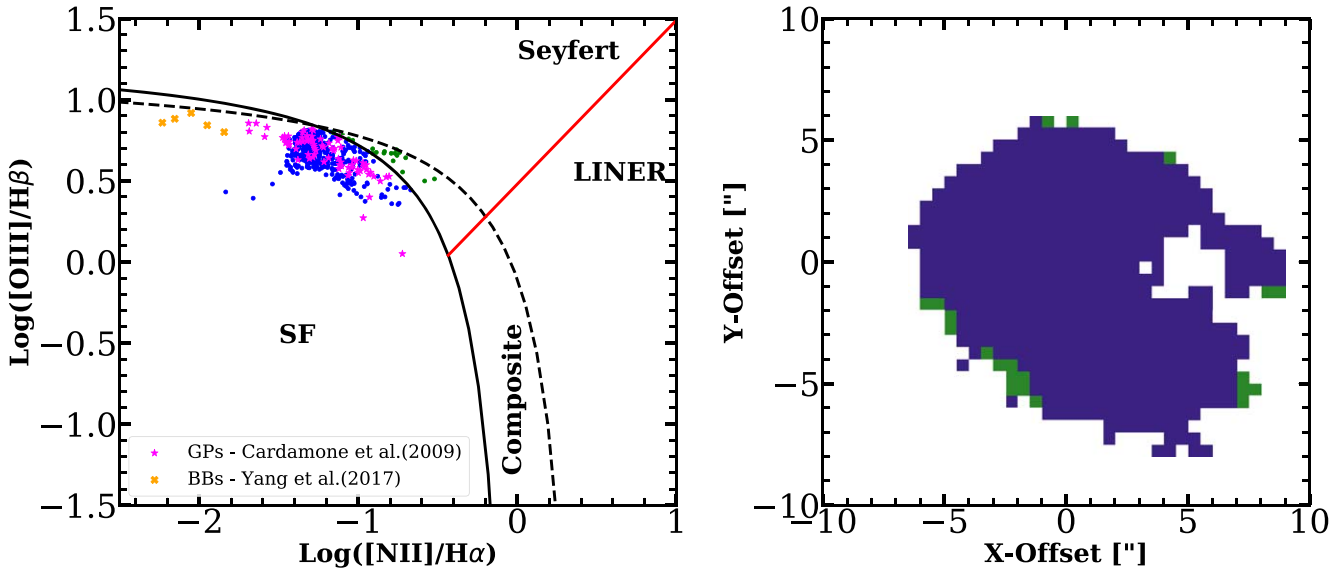

Figure 2. Left: the BPT diagram based on the [N II] $\lambda6583/H\alpha$ vs. [O III] $\lambda5007/H\beta$ emission-line ratios, labeled with different regions corresponding to star formation (SF), active galactic nucleus (AGNO/shock (Seyfert or LINER), and composite (AGN+SF) processes. The GPs and blueberries from the literature (Cardamone et al. 2009; Yang et al. 2017a) are shown by the star and cross symbols, respectively. The spaxels from our blueberry galaxy are shown by blue dots. Right: corresponding to the left figure, the color-coded 2D spatially resolved BPT diagram of our blueberry galaxy.

other GPs and blueberry galaxies, the central bright compact region of our identified blueberry system as marked by the dashed circle in Figure 1(d) shows a high value of [O III]/[O II] $\gtrsim 10$. The values of [O III]/[O II] drop off sharply as one moves outward, reaching nearly zero at the outskirts of the galaxy, indicating that the outer part is likely dominated by old, low-mass stars.

3.1. Spatially Resolved BPT and Other Physical Properties

In this section, we first derive the spatially resolved Baldwin, Phillips, & Terlevich (BPT; Baldwin et al. 1981) diagnostic diagram to understand the nature of the galaxy spaxel-wise. Spaxels are selected only when their emission lines such as [O III], Hα, [N II], and Hβ have S/N $\geqslant 3$. The BPT diagram (shown in Figure 2) indicates that most spaxels either from the blueberry or the LSB-disk region fall in the star formation region, confirming their nature as a star-forming galaxy. Nearly all the spaxels belonging to the blueberry and LSB disk also overlap with the region occupied by other GPs and blueberries available in the literature. This, in other words, confirm that SHOC 579 is not a host to an active galactic nucleus.

Because blueberries and GPs are, in general, very compact, a spatially resolved study of these galaxies using SDSS data alone is not possible. Thanks to the MaNGA IFU data and the close proximity of the blueberry galaxy in this study, they allowed us to analyze the spatially resolved spectroscopic properties for the first time. We construct the 2D spatial distribution of the EW(Hα), EW([O III] $\lambda5007$), $E(B-V)$, and $12+\log(O/H)$ parameters using the MaNGA maps as shown in Figures 3 (a)–(d). In these figures, the blueberry region is marked by the dashed circle. The EWs of the Hα and [O III] $\lambda5007$ emission lines are directly derived from each spatial spaxel in the MaNGA datacube as discussed in Section 2. The extremely high values (>1200 Å in the observed frame or <1146 Å in the rest frame) of EWs of [O III] and Hα in the blueberry region suggest the dominance of a very young stellar population over the older ones and ongoing starburst activity. The rest of the galaxy, i.e., the disk-like region, appears to be like a normal star-forming galaxy. While the central region of the blueberry component is dusty, showing $E(B-V)\simeq 0.2$ or above, the rest of the galaxy is almost dust free, having $E(B-V)<0.1$.

The metallicity map (shown in Figure 3(d)) is derived using the so-called N2 method (Pettini & Pagel 2004),

$$12+\log(O/H)=8.90+0.57\times\log([N\,II]\lambda6583/H\alpha). \quad (1)$$

The metallicity map clearly shows that the blueberry region has a subsolar metallicity. The northeast corner is slightly metal poor compared to the rest. Note that this is also the region having the least amount of dust (as seen in the $E(B-V)$ map). The rest of the galaxy is also at subsolar metallicity, except the southern edges of the galaxy that show relatively metal-rich regions.

3.2. Stellar Mass and Star Formation Main Sequence

Here we characterize the stellar properties of the blueberry and its extended host galaxy by modeling their spectral energy distribution (SED). A multiwavelength broadband SED (1300 −45000 Å) is constructed by estimating the photometric fluxes from the far-ultraviolet (FUV) GALEX (Martin et al. 2005) to the infrared (IR) from the Spitzer survey (Dale et al. 2009). Because the multiband observations are taken with telescopes having widely varying point-spread functions (PSF), we employ a PSF-matching technique (Becker et al. 2012) to estimate the fluxes from the central blueberry region and the full galaxy (see Appendix A for details). The resulting SED is modeled with the Python Code Investigating GALaxy Emission (PCIGALE; Boquien et al. 2019) (details are provided in Appendix B). The best-fit SED model, presented in the left panel of Figure 4, has a $\chi^2_{\rm reduced}=8.0$ and 5.2 for the full-galaxy model and blueberry component, respectively. Note that our full-galaxy model deviates considerably from the data on the high-wavelength side, especially in two Spitzer bands. Our best-fit model SED yields a total stellar mass of $5.2\times10^9\ M_\odot$ and $4.5\times10^8\ M_\odot$ for the full galaxy and the blueberry component, respectively. Note that the stellar mass of the

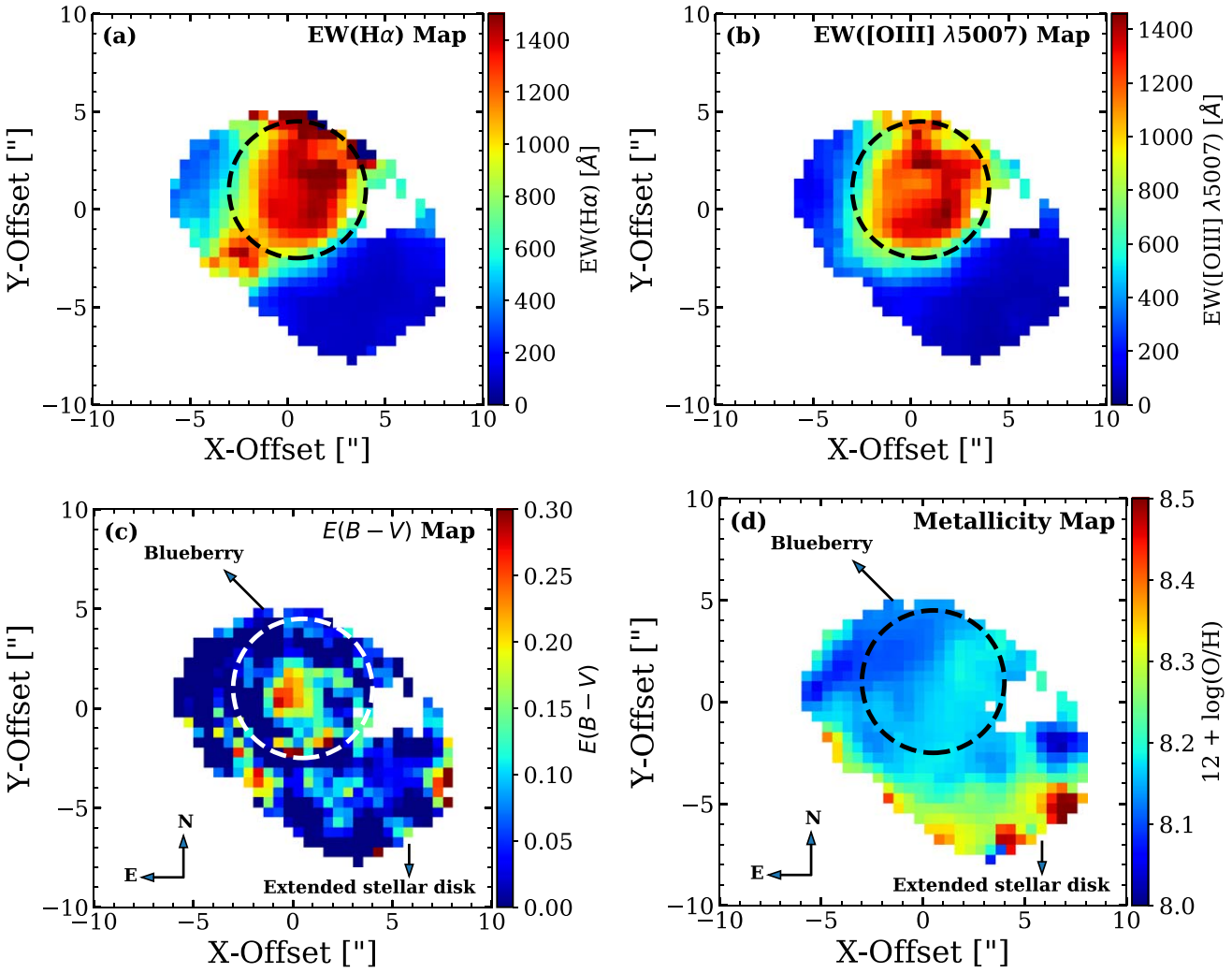

Figure 3. The spatially resolved 2D maps of the (a) EW(Hα), (b) EW([O III] λ5007), (c) $E(B-V)$, and (d) 12 + log(O/H) of our galaxy in this work. The dashed circle in each figure indicates the spatial extent of the blueberry region in the galaxy.

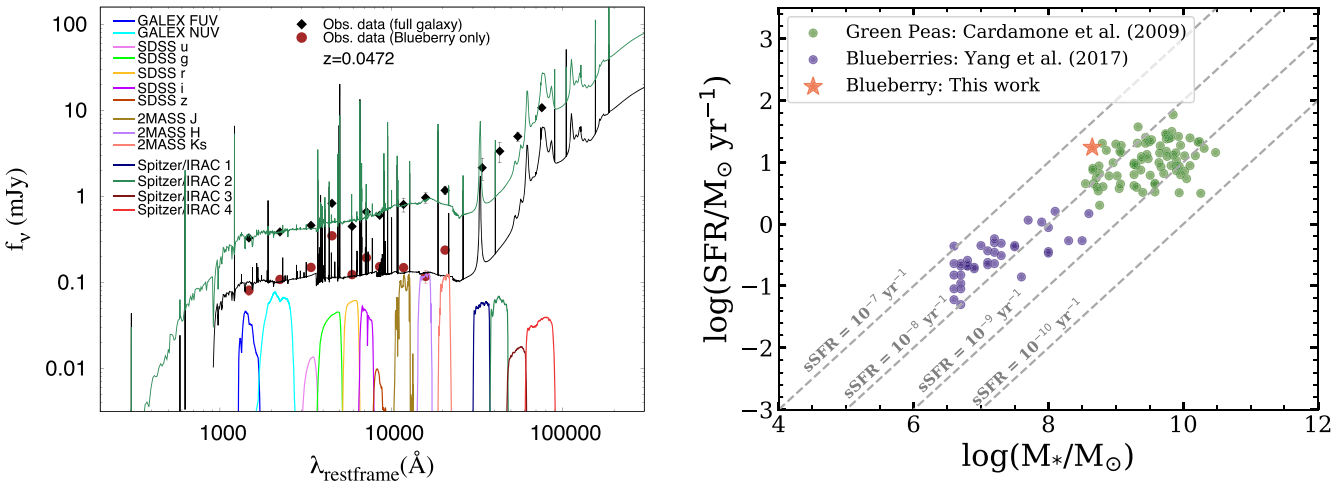

Figure 4. Left panel: multiwavelength SED modeling—the black diamond and red circle points represent the photometric band fluxes from FUV to IR for the full galaxy and the blueberry component only, respectively, obtained using PSF-matched images (see Section A). The corresponding SED spectra for the full galaxy and blueberry component are shown by the green and black solid lines, respectively. The error bars denote 1σ uncertainties on the measured fluxes. Right panel: the main-sequence relation for blueberries and GPs. The blueberry in this work is shown by the star symbol. Other blueberries and GPs studied in the literature (Cardamone et al. 2009; Yang et al. 2017a) are represented by blue and green solid circles, respectively. Several dashed straight lines show different MS relations at constant sSFR from 10^{-7} to 10^{-10} yr^{-1}.

blueberry component is only about 8% of the full galaxy, consistent with that observed in the case of GPs (e.g., Amorín et al. 2012). This is the most massive blueberry similar to GPs known to date (Cardamone et al. 2009; also see the right panel of Figure 4), although this is as compact (with $R_e \sim 217$ pc as estimated in Section 4) as other locally known blueberries.

Based on our SED modeling, we find that the SFR, averaged over 10 Myr of the SFH, of the full galaxy is $\sim 15.1\, M_\odot\ \mathrm{yr}^{-1}$, whereas the extinction-corrected Hα SFR in the blueberry region is found to be $\sim 17.4\, M_\odot\ \mathrm{yr}^{-1}$—this is the highest-SFR blueberry among the local blueberries known so far. The mass-weighted age of the stellar population in the blueberry component and the full galaxy are 5.6 Gyr and 7.05 Gyr, respectively. Our SED age estimates are comparable to those obtained from the pPXF fitting of the stacked spectra from either region (see Appendices B and D for further details). The right panel of Figure 4 shows the star-formation–main-sequence (MS; M_*−SFR) relation for our blueberry galaxy and a comparison with other blueberries and GPs in the literature (Cardamone et al. 2009; Yang et al. 2017a). The stellar mass of the blueberry in this work is obtained from our SED analysis (see Section B), while the SFR is derived using the dereddened Hα luminosity from each spaxel of the galaxy, following the relation (Kennicutt 1998)

$$\mathrm{SFR}(M_\odot\ \mathrm{yr}^{-1}) = 7.9 \times 10^{-42} L_{\mathrm{H}\alpha}(\mathrm{erg\ s}^{-1}) \quad (2)$$

The estimated SFRs from each spaxel are then integrated to estimate the total SFR. On the right panel of Figure 4, we see that blueberries and GPs from the literature are higher by ∼2–3 orders of magnitude in terms of sSFR compared to normal star-forming galaxies (represented by the constant sSFR line $10^{-10}\,\mathrm{yr}^{-1}$); our blueberry galaxy is not an exception to this. This implies that the typical mass-doubling time for GPs and blueberries is between 100 Myr and ∼1 Gyr. The blueberry galaxy SHOC 579 studied in this work is consistent with these timescales.

3.3. Comparison with Other GPs and Blueberries

Figures 5 (a)–(d) show the comparison of various physical parameters of SHOC 579, such as EW [O III] λ5007, [O III]/[O II] ratio, nebular color excess, and metallicity of the blueberry component (i.e., within the dashed circle), with previously known GP and blueberry galaxies available in the literature (e.g., Cardamone et al. 2009; Yang et al. 2017a). While these parameters for the GPs and blueberries from the literature are derived using the aperture-integrated light obtained with slit observations (i.e., the SDSS and MMT spectroscopic observations), the same for our blueberry component is represented by the median values of all the spaxels within the dashed circle as shown in Figure 3. Our obtained median values of EW [O III] λ5007, [O III]/[O II] ratio, and $E(B-V)$ are similar to those of other typical GPs and blueberries, except the metallicity. The median metallicity of our blueberry component has an intermediate value, lying between the typical blueberries and GPs. In other words, our blueberry is metal poor compared to GPs and metal richer compared to blueberries. In terms of stellar mass, our blueberry is similar to typical GPs (see right panel of Figure 4). Overall, our comparison implies that the galaxy in this study represents the most metal-rich and massive blueberry source.

4. 2D Modeling of the Surface Brightness Distribution

We carried out a detailed 2D modeling of the galaxy using GALFIT (Peng et al. 2002). In that, we model the central bright component using a Sérsic profile (Sersic 1968) while the extended faint stellar envelope was modeled with an exponential profile. The best-fit models and residuals are displayed in Figure 6. The details of our GALFIT modeling is presented in Appendix C Based on the two-component modeling of the SDSS *i*-band image of the galaxy, we arrive at an insight revealing the nature of the galaxy's light distribution. The best-fit model of the extended host galaxy reveals a faint, lopsided, LSB exponential profile that is presumably due to an old stellar host. The presence of an exponential profile as found in many BCDs (e.g., Papaderos et al. 2002; Lian et al. 2015), as well as in SHOC 579, is not convincing enough for a thin stellar disk; possibilities of a triaxial stellar system cannot be ignored. The central surface brightness of the disk is $\mu_0 = 22$ mag arcsec^{-2} (e.g., Brown et al. 2001; Schombert et al. 2001; Adami et al. 2006; Pahwa & Saha 2018) with a scale length of $R_d = 1.54$ kpc. Note that the disk is relatively smaller in size and the scale length is similar to that of dwarf LSB galaxies (Schombert et al. 1995; Papaderos et al. 1996b; Schombert et al. 2001; Gil de Paz & Madore 2005). The Sérsic profile for the inner component has a Sérsic index of $n = 1.48$ and an effective radius of 217 pc. Because our GALFIT modeling is performed using the SDSS *i*-band image, it hence does not contain strong nebular emission lines (e.g., Hα line) for the given redshift of the galaxy. Nevertheless, the contributions from the nebular continuum cannot be ruled out. In fact, the contribution from the nebular continuum has especially been found to be significant in the SDSS *i*-band image (e.g., Izotov et al. 2011). Therefore, an exponential light distribution indicating a stellar-disk-like structure around the blueberry source may be a generic property of an extended nebular halo, similar to that seen in several luminous BCDs (e.g., Papaderos et al. 2002).

We compare the structural properties of the blueberry host galaxy with those of local dwarf galaxies, including LSB, GP, and XBCD systems (see Figure 7). Because the image of SHOC 579 is not available in the Johnson *B*band, the values of the central surface brightness ($\mu_{E,O}$) and absolute magnitude (M_B) of our blueberry host in the *B* band are therefore derived using the SDSS images in the *g* and *r*bands, after applying the Lupton transformation relations published on the SDSS DR4 website. Note that the derived values of $\mu_{E,O}$ and M_B have been corrected for Galactic extinction. In Figure 7, it can be clearly seen that our blueberry, along with GPs, falls in the same parameter space that is populated by luminous BCDs. This result suggests that all these galaxy classes have common structural properties, and an extended disk-like structure in starburst dwarf galaxies such as blueberries, GPs, and XBCDs might be a general rule. Alternatively, this result also implies that, with respect to the structural properties of their host galaxies, blueberries and GPs pass through a common evolutionary track along with the main population of BCDs, except for their extreme emission-line properties observed due to their strong starburst phase. Their strong starburst phase is likely due to an occasional event whose triggering mechanism needs to be explored in detail.

In the context of the above discussion, it is worth mentioning that the possibility of a very faint old stellar disk in the blueberry host cannot be dismissed. A detailed analysis of structural properties of CELLs (i.e., blueberries and GPs) host galaxies using near-infrared (NIR) images having a spatial resolution of subkiloparsec scale (e.g., observations of CELLs galaxies with

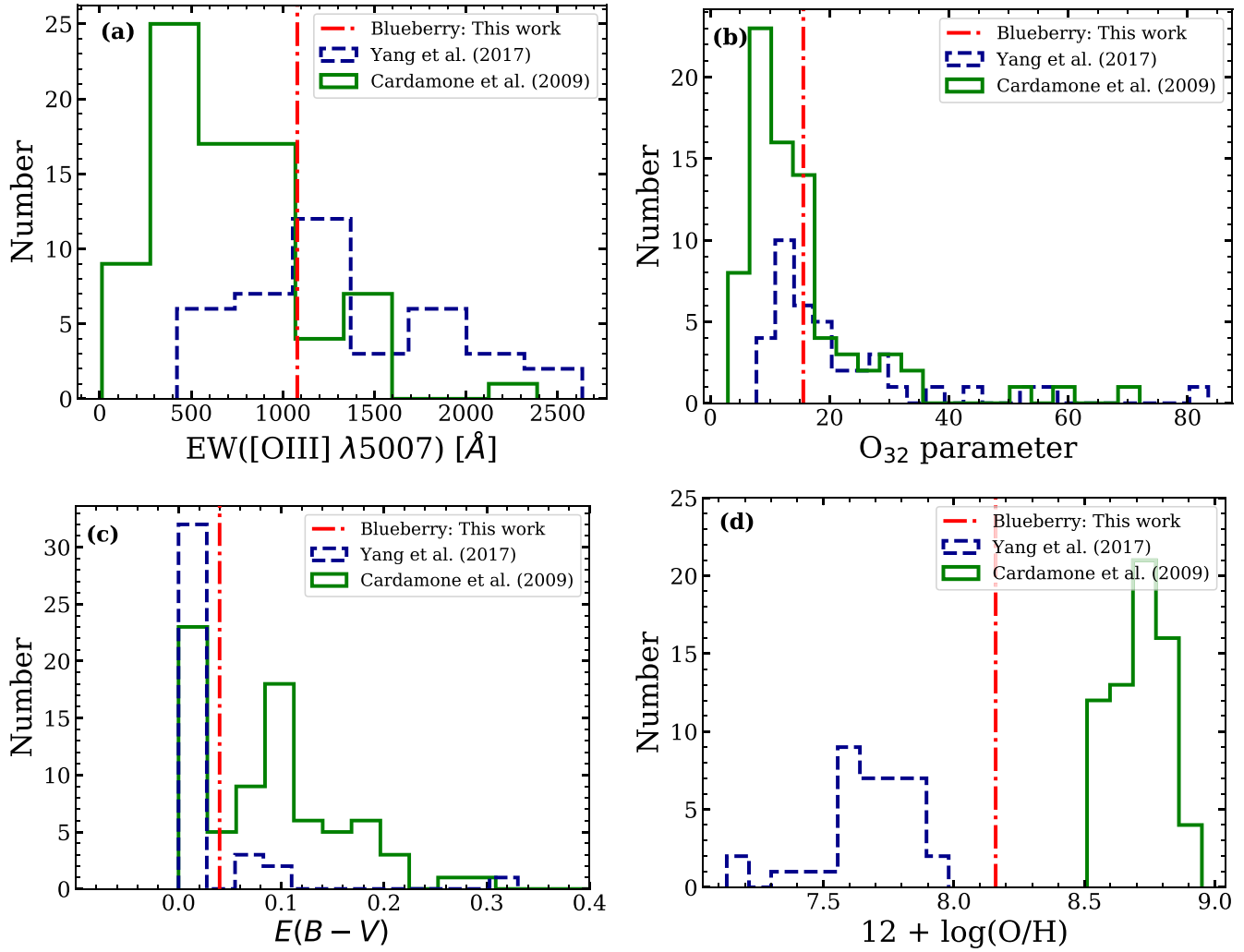

Figure 5. The histograms of (a) EW([O III] λ5007), (b) O_{32} parameter, (c) $E(B-V)$, and (d) 12+log(O/H) of GPs and blueberries studied in the literature (Cardamone et al. 2009; Yang et al. 2017a), represented by green solid and blue dashed lines, respectively. The median values of the same parameters estimated over the blueberry region of SHOC 579 are shown by the vertical red dotted–dashed line.

JWST) may further shed light on the existence of old stellar disk. Such studies with the NIR images could also reveal additional stellar masses distributed over larger radii.

5. Evidence of an Old Stellar Population

Figure 8 presents a clear detection of the Mg I λ5173,5167 absorption line in the central blueberry region as well as in the LSB disk. The Mg I λ5173,5167 absorption line is generally seen in the late-type stars and is an excellent tracer of α abundances in a galaxy. Its detection in the galaxy's spectrum provides us with the confirmation of the presence of old stars (e.g., Amorín et al. 2012). However, the Mg I λ5173,5167 absorption lines are too weak to be detected in the spatially resolved spaxel in the galaxy. Even in the SDSS 3″ fiber spectrum centered on the blueberry region, our search resulted in a weak detection (below 3σ; see Figure 8(d)). It is only after stacking the MaNGA spectra from both the blueberry and the LSB-disk regions (for details, see Appendix D) could we reveal the detection with confidence. In Figures 8(b) and (c), we show the Mg I λ5173,5167 absorption feature detected with a significance of 6σ and 5σ in the blueberry and disk region, respectively, indicating clear evidence of an underlying old stellar population in the blueberry region. This is thanks to the MaNGA IFU observations (Bundy et al. 2015) with a large integration time of ∼8100 s that made detection possible. In fact, this is the first time we observationally establish a clear existence of an old stellar population simultaneously in the blueberry region and in the surrounding LSB disk using IFU spectroscopic data. Future IFU observations of other blueberries and GPs would be a useful path to unravel their true stellar population content. It is worth mentioning here that a very recent study based on the resolved structure and color deduced with the newly acquired HST imaging observations has also revealed evidence of old stellar populations (>1 Gyr) in a set of nine GP galaxies (Clarke et al. 2021).

We further made effort to detect the Mg I λ5173,5167 absorption feature in a gradual spatially resolved manner after stacking the spectra from 5×5 spaxels over the whole galaxy extent (e.g., see the left panel in Figures 10(a1)–(a11)). We selected 5×5 spaxel stacking because it gives us spectral information over a spatial region of 2.″5 that is equivalent to SDSS fiber-slit aperture and also to the effective spatial resolution of the MaNGA survey (i.e., 2.″5 FWHM). In this manner, we find a weak (below 3σ) detection of Mg I λ5173,5167 absorption, except for a few regions in the LSB disk and central blueberry region. Nevertheless, the presence of a weak Mg I λ5173,5167

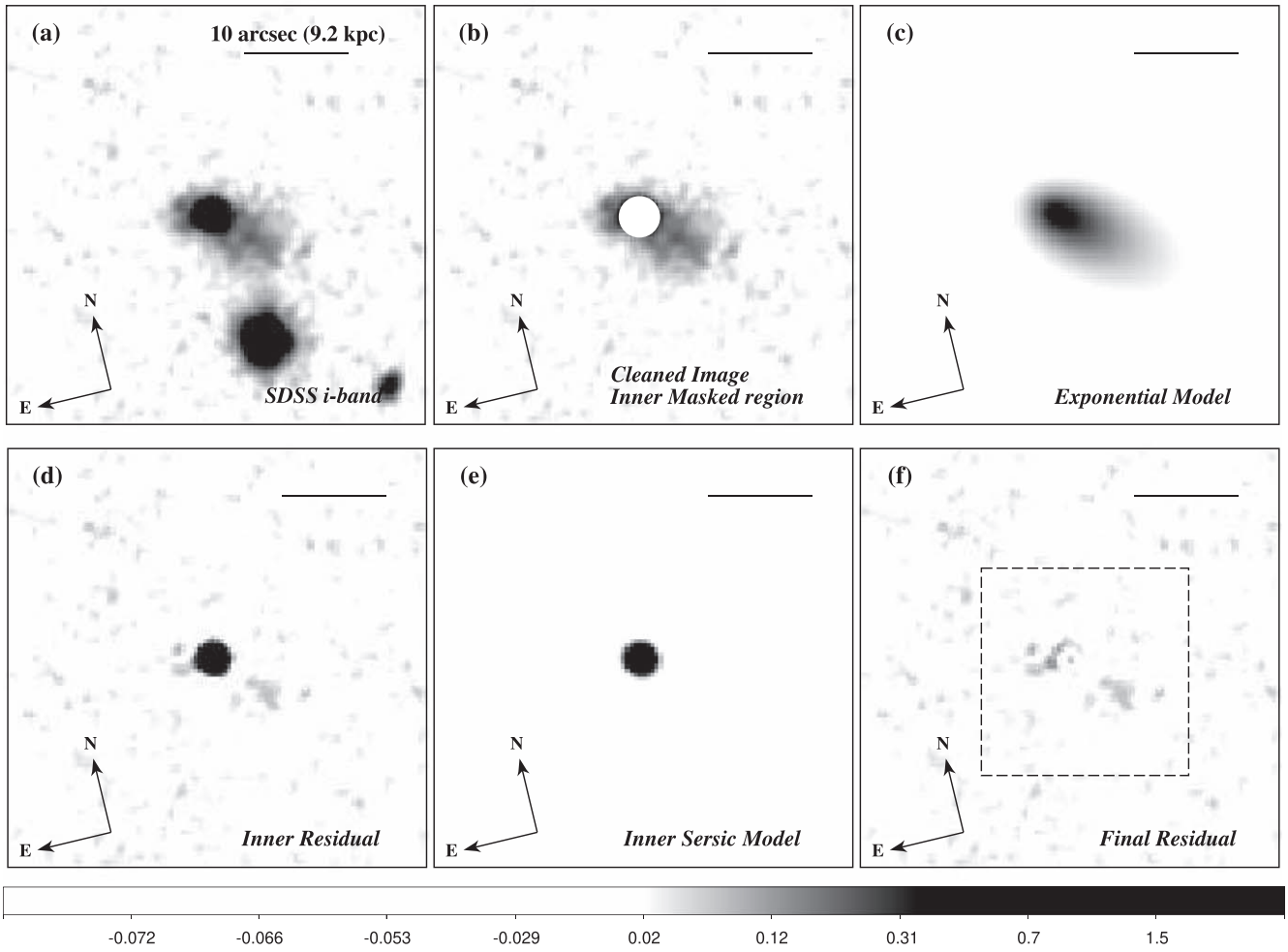

Figure 6. (a) The observed SDSS *i*-band image of the target galaxy. (b) The cleaned (nearby sources removed) parent image of the source used for 2D fitting. Here, the inner central region has been masked with a circular aperture of radius $\sim 2''$ while fitting the 2D exponential disk (for details see text). (c) The modeled lopsided exponential disk. (d) The central bright component of the galaxy obtained as a residual, after subtracting the modeled exponential disk from the observed galaxy. (e) The modeled Sérsic component to the inner/central region of the galaxy. (f) The final residual image after subtracting the complete galaxy model from the observed galaxy. The dashed box here represents the region occupied by the source in the parent image. In each image, a common scale limit and contrast bias are used. The color-bar units are in nanomaggy.

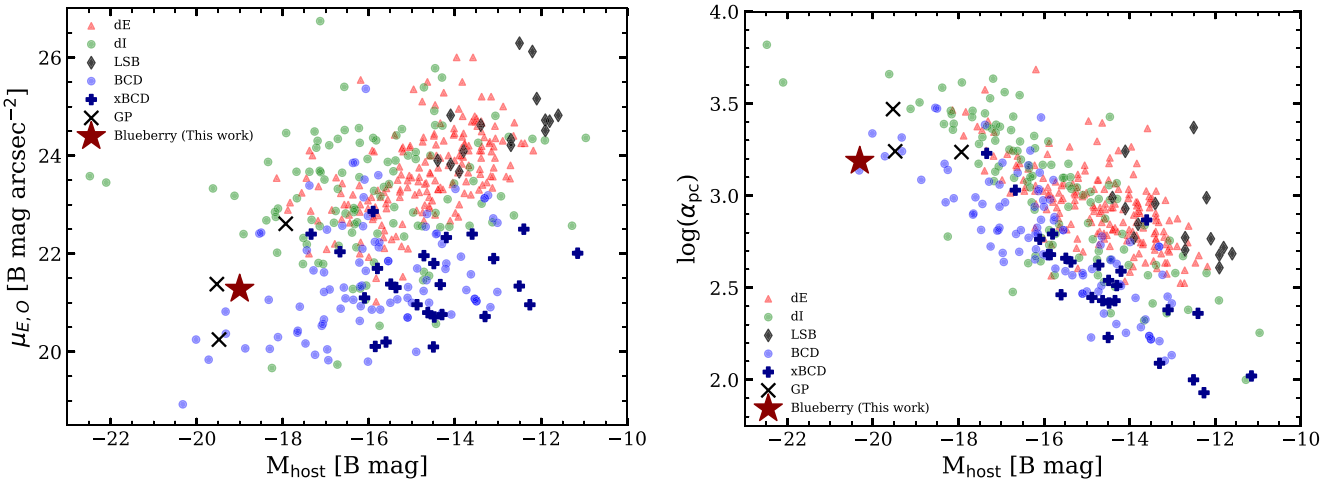

Figure 7. Comparison of the structural properties of the host LSB galaxy of the blueberry (as shown by the star symbol) with other classes of low-mass dwarf galaxies such as dwarf elliptical (dE), dwarf irregular (dI), BCD, XBCD, and LSB taken from Papaderos et al. (2008), including three GPs from Amorín et al. (2012). The left and right panels compare, respectively, the central surface brightness and the exponential scale length vs. the absolute magnitude of the LSB host galaxy of different classes of dwarf systems. The respective symbols for representing the galaxy of different types are shown in the legends.

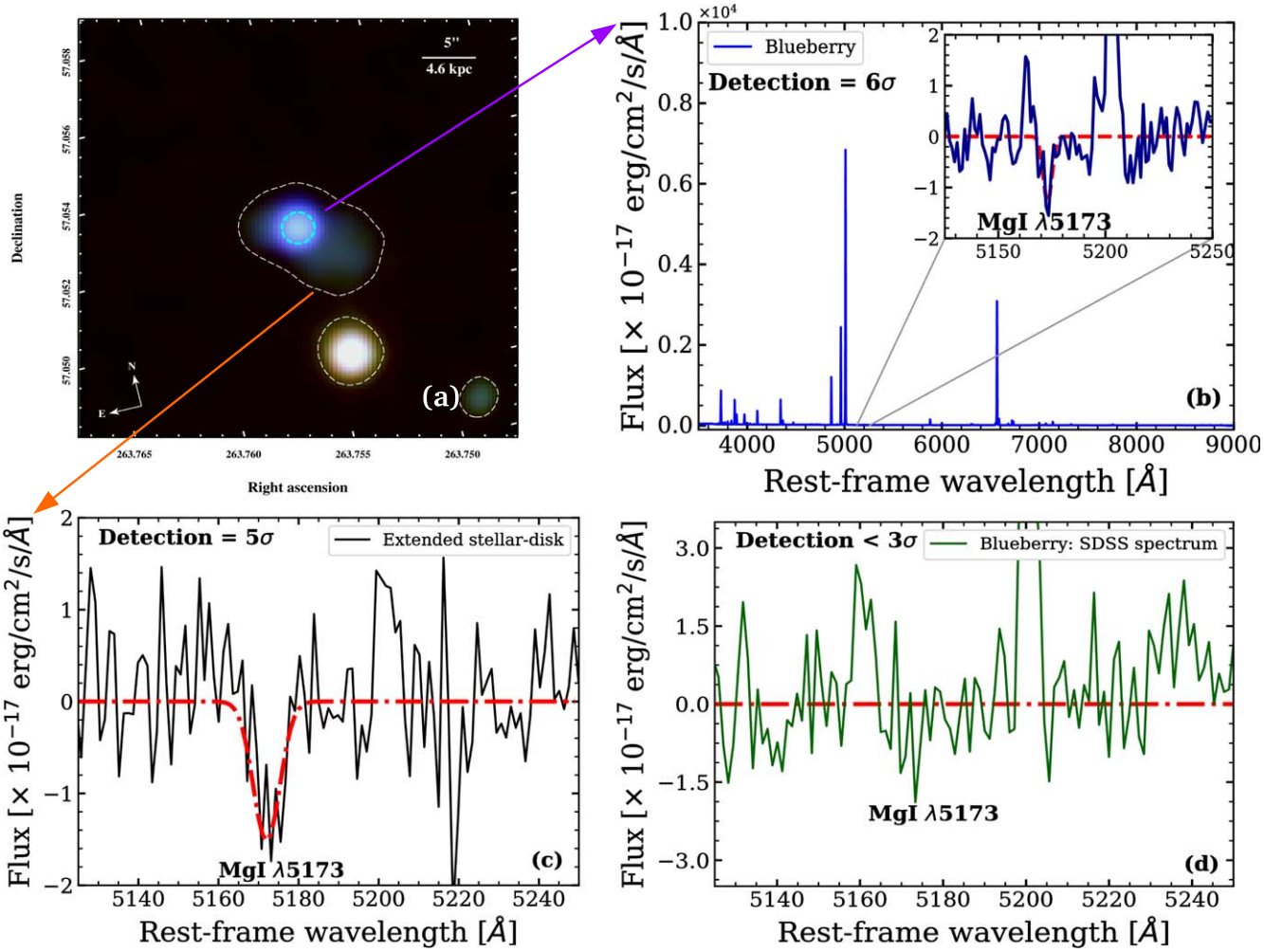

Figure 8. (a) The *gri*-band color composite image of SHOC 579. The dashed line shows the contour at 3σ level above the background. The inner dashed circle of size 3″ (diameter) marks the blueberry region. (b) The stacked full observed spectrum within a 3″ diameter. The inset represents the detection of the Mg I λ5173 absorption line from the blueberry region. (c) The detection of the Mg I λ5173 absorption line obtained through the stacked spectra from the extended diffuse stellar-disk region. (d) Null detection of the Mg I λ5173 absorption line in the observed SDSS spectrum taken over the central 3″ diameter on the blueberry region. In each spectrum, the red dashed line represents the fitted continuum + Gaussian models over the observed Mg I λ5173 absorption feature. In panel (d), the Gaussian model is not fitted as the detection of the Mg I λ5173 absorption feature is below 3σ.

spectral feature throughout the galaxy extent suggests that our blueberry host galaxy contains a very faint and widespread old stellar population. Whether the stellar disk with the old stellar population is rotation supported is addressed in Section 6. Our analysis at this stage provides a clue that there might exist an underlying old stellar disk in CELLs galaxies, and it further demands a detailed exploration with a large sample of CELLs galaxies with better-quality data.

Intriguingly, the metallicity of the blueberry region is only subsolar, which is obtained as $Z \sim 0.008$ from our SED analysis. The SED-based metallicity is consistent with the N2-based metallicity map derived from the MaNGA observation for a solar [O/Fe] ratio (see Figure 3(d)), while the disk is at about solar metallicity. Based on our pPXF fitting over the stacked spectra of the extended LSB-disk component (see Appendix D), we obtain its mass-weighted mean stellar age as ∼7.4 Gyr. Similarly, it is found to be ∼5 Gyr old in the case of the blueberry component. The age of the recent starburst event observed with the Hα-based SFR of ∼17.4 $M_{\odot}\,\mathrm{yr}^{-1}$ is ⩽10 Myr old. This age for recent starburst events is mainly constrained by the detection of a broad Wolf–Rayet (WR) feature along with He II λ4686 emission only from the blueberry component (see Paswan et al. 2022). The WR feature generally appears in a galaxy due to the presence of a substantial (10^2–10^5) population of WR stars (e.g., Kunth & Sargent 1981; Kunth & Schild 1986) whose progenitors are evolved massive O-type stars. These O-type stars come to the WR phase 2–5 Myr after their birth, spending a very short time in this phase (Meynet & Maeder 2005) before ending their life through supernova explosions. Therefore, the detection of the WR phase constrains the age of recent starburst events in a galaxy. Overall, our stellar-age analysis suggests that the blueberry galaxy in this study has experienced multiple episodes of star formation, similar to the typical class of dwarf galaxies (e.g., Thuan et al. 1991; Krueger et al. 1995; Thornley et al. 2000; van Zee 2001). Furthermore, the detection of the WR feature in our blueberry also suggests that this galaxy harbors hard-ionization radiation fields. This is consistent with our observed high [O III]/[O II] emission-line ratio (see Section 3), showing one of the primary emission-line properties of a typical CELLs galaxy (e.g., Cardamone et al. 2009; Yang et al. 2017a).

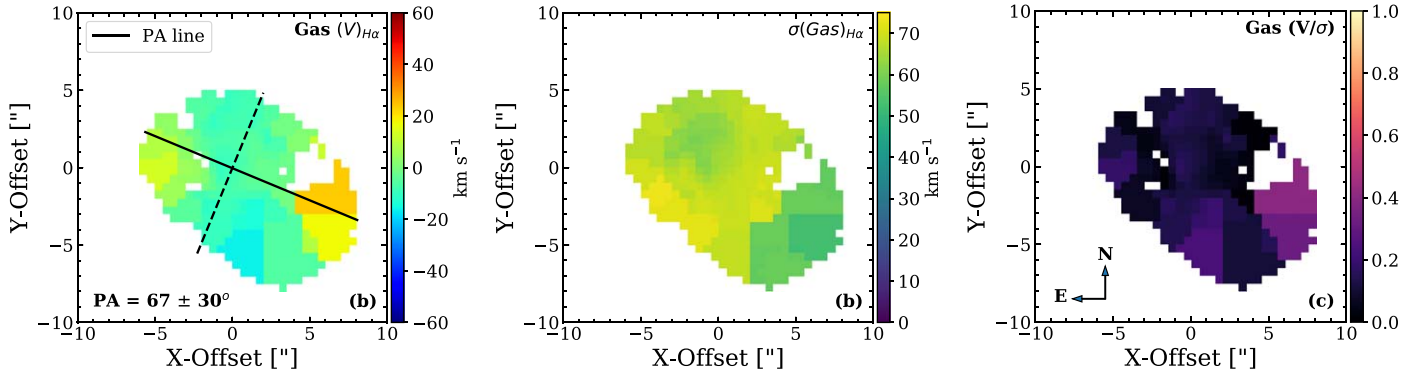

Figure 9. Plots representing the gas kinematics. Panel (a) shows the rotation velocity of the ionized gas traced using the Hα emission line. In this panel, solid and dashed lines represent the major and minor kinematic rotation axes of the gas component, respectively. Panels (b) and (c) represent the gas velocity dispersion (σ) maps and V/σ maps of gas, respectively.

6. Stellar and Gas Kinematics

The spatially resolved kinematics of stars and gas in blueberry galaxies (or even in GPs) has largely remained unexplored, primarily due to the unavailability of IFU observations. In this light, MaNGA data of SHOC 579 represent the first IFU observation of a blueberry galaxy. The gas kinematics (see Figure 9) of the galaxy is derived using the strong Hα emission line (corrected for instrumental broadening). However, only stellar kinematics could be obtained in a limited sense using the stellar Mg I λ5173,5167 absorption line. The full galaxy is divided into 11 bins, each with 5×5 spaxels. The left panel of Figure 10 shows the stacked spectra from each of these 11 bins. The bins marked by a3, a5, a9 a10, and a11 have S/N $\geqslant 3$. Note that the same was not possible with the stellar hydrogen absorption lines because these lines were too weak to be detected in the spatially resolved manner, even after stacking the spectra from 5×5 spaxels. Other stellar absorption features (e.g., Ca II λ8498,8542,8662, etc.) were not detected in the spectra.

We fit the Gaussian models to only those Mg I λ5173,5167 absorption lines detected with S/N > 1.5 as shown in the left panel of Figure 10, and then derive the stellar line-of-sight velocity and dispersion. The derived stellar velocity dispersion is corrected for the instrumental broadening. The final stellar kinematics is shown in the right panel of Figure 10. Thanks to the MaNGA IFU observation and the proximity of SHOC 579 to us, it allowed us to derive the first stellar and gas kinematics of a blueberry galaxy in the literature. The left panels of Figure 10 show the velocity, velocity dispersion, and stellar $(v/\sigma)_{\rm los}$ from each bin. From Figures 10 and 9, it can be seen that the identified LSB disk in our blueberry galaxy does not seem to have a well-defined rotation pattern, both in stars and gas. Although the gas velocity pattern merely follows that of stars, gas seems to be rotating slower than the stars. They also appear to be misaligned by $\sim 30^{\rm o}$, estimated based on the PA fit module (Cappellari & Emsellem 2004). The observed $(v/\sigma)_{\rm los}$ map traced by the ionized gas suggests that the entire galaxy is rather pressure supported, similar to high-z galaxies (Newman et al. 2013) while the stellar $(v/\sigma)_{\rm los} \simeq 1$ or so in the disk—a slight indication of rotational support. It is worth mentioning here that prior to this study, Lofthouse et al. (2017) have reported the gas kinematics of four GPs, wherein they found two GPs with pressure-supported kinematics and two that are rotation supported.

In summary, our gross kinematic structure suggests a low-angular-momentum content in the galaxy; it might be possible that the disk has lost a good fraction of its angular momentum during the recent strong stellar feedback due to the starburst event (Ferrara & Tolstoy 2000; D'Onghia et al. 2006; Scannapieco et al. 2008; Genel et al. 2015). But this needs to be proven. On the other hand, it might be the case that we have been witnessing the recent kinematic settling of an exponential LSB disk (Kassin et al. 2012) in this low-mass starburst galaxy. Nevertheless, readers are cautioned that the finding of an exponential surface brightness profile (as shown in Section 4) with a mildly rotation-supported stellar kinematics alone is not compelling evidence of a thin stellar disk in dwarf systems because the possibility that the LSB host of SHOC 579 is a triaxial stellar system, similar to other BCDs and dwarf ellipticals, cannot be discarded (e.g., Sung et al. 1998; Papaderos et al. 2002). In the literature, it is still a debated issue whether dwarf systems indeed host a stellar disk or triaxial stellar system. It is apparent that there is a need for high-resolution IFU spectroscopy covering the full galaxy to establish the true kinematic state and whether the blueberry host contains a disk or a triaxial stellar system firmly.

7. Discussion and Conclusions

In the present work, we show the structural properties of a special class of objects, the so-called blueberry galaxy, at $z \sim 0.0472$. Using its SDSS *i*-band image, we perform GALFIT modeling that reveals an exponential LSB-disk-like structure around the blueberry region, presumably due to an old stellar disk. However, we could not rule out if this is a generic property of nebular halos. With the help of MaNGA IFU data, our hypothesis on the presence of a faint old stellar disk is partially supported by the detection of Mg I λ5173,5167 over the entire galaxy extent. The stellar kinematics indicates the presence of rotation support in the galaxy. Such kinematics with limited data quality, however, could not rule out if it is a triaxial stellar system. Overall, our results suggest that the blueberry galaxy in this study has similar structural properties (see Figure 7) and SFHs (containing stars from old, intermediate to young ages) to those seen in other typical starburst dwarf galaxies, e.g., BCDs (e.g., Papaderos et al. 1996a, 1996b; Thornley et al. 2000; Cairós et al. 2001; van Zee 2001; Noeske et al. 2003; Guseva et al. 2004; Gil de Paz & Madore 2005; Papaderos et al. 2008). Nevertheless, this class of objects is unique because of their extreme emission-line properties and strong starburst events similar to high-redshift, compact,

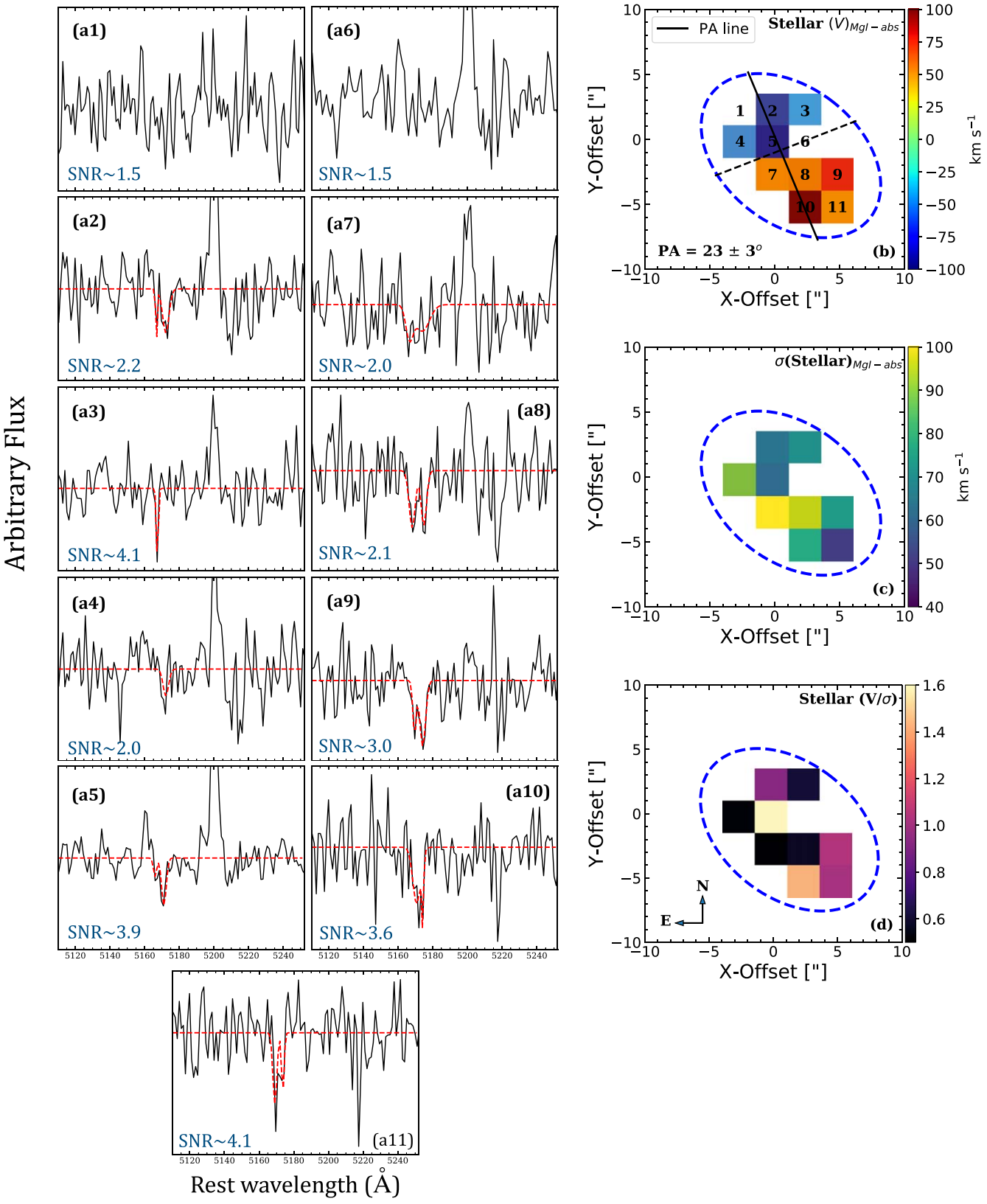

Figure 10. Left panels: a1—a11 show the spectra for the detection of the Mg I λ5173,5167 absorption line. Each spectrum is derived after stacking the spectra from all possible 5 × 5 MaNGA spaxels over the galaxy extent as denoted by the dashed blue ellipse in the right panel. Here, each 5 × 5 binned spaxel is represented by a single spaxel and numbered according to its corresponding 1D spectra (a1–a11). The Gaussian models (red dashed lines) are only fitted over the 1D spectrum showing the line detection with S/N above 1.5. In the right panel, (b) shows the stellar line-of-site (LOS) rotation velocity (V) derived using the stellar Mg I λ5173,5167 absorption line. Here, the solid and dashed lines represent the major and minor kinematic rotation axes of the stellar component, respectively. Similarly, (c) and (d) show the velocity dispersion (σ) and V/σ maps of the stellar component.

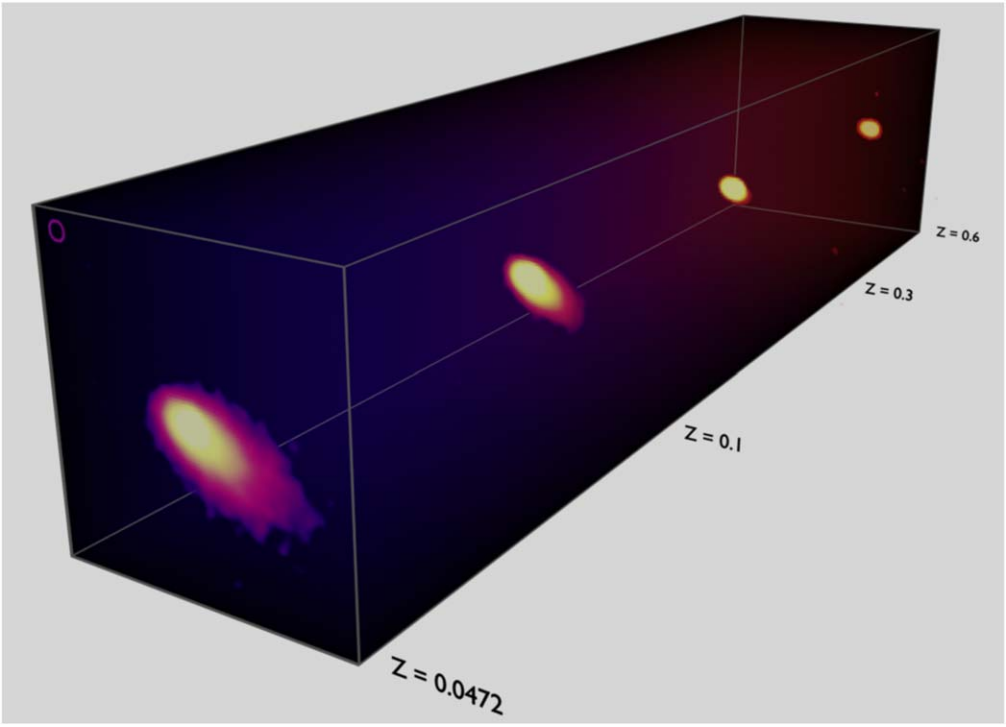

Figure 11. The 2D image visualization of our galaxy in this study at different redshifts from 0.0472 to 0.6. The circle shown at the front upper-left corner denotes the SDSS (FWHM $\sim 1\farcs2$) beam size.

starburst LyC and Lyα emitters (e.g., Jaskot & Oey 2014; Henry et al. 2015; Yang et al. 2016, 2017b; Verhamme et al. 2017; Izotov et al. 2021).

Our current results on blueberries, including the work by Amorín et al. (2012) and Clarke et al. (2021) on GPs, reveal that CELLs galaxies are luminous counterparts of local starburst dwarf galaxies such as BCDs. Therefore, the presence of an LSB disk in these objects might be a general rule, similar to BCDs; however, it is not clearly seen in most of the cases using a ground-based SDSS-like survey. Perhaps, it became possible in our case due to the proximity of our blueberry source (at $z \sim 0.047$) and the observed stellar mass of its LSB disk (i.e., $4.75 \times 10^9\ M_\odot$) whose surface stellar mass density is well above the SDSS detection limit. This detection limit is defined as $\sim 10^6\ M_\odot\ \mathrm{kpc}^{-2}$, assuming $M_r/L_r = 1$ (Kauffmann et al. 2003) with a typical integration time of 50–100 s (York et al. 2000; Gunn et al. 2006).

It is worth discussing here how a faint extended stellar disk in a CELLs galaxy situated at a relatively higher redshift might be missed by SDSS-like surveys. For this, we performed an exercise on the dimming effect in our blueberry galaxy's image, after putting its 2D model images at various redshifts from $z = 0.0472$ to $z = 0.6$. In this exercise, at all redshifts, we varied the apparent intensity of our source by a factor depending upon redshift, $(1 + z)^{-4}$, an effect known as redshift dimming or Tolman dimming (see Tolman 1930, 1934; Hubble & Tolman 1935). In the redshifted model images, we added Poisson noise in combination with the SDSS background noises so that the model images mimic the observed SDSS images. Note that as the source moves toward higher redshifts, its angular size will vary following the cosmological scale parameter in units of kpc arcsec^{-1}. Assuming the SDSS plate scale (i.e., $0\farcs396\ \mathrm{pixel}^{-1}$; Gunn et al. 1998) and physical size of the source in the units of kpc, we took care of the variation in angular size of the galaxy images at different redshifts. A visual demonstration of the redshift dimming of our galaxy is presented in Figure 11. It can be seen that the underlying LSB disk starts disappearing into the background noise beyond redshift 0.1 or so. This implies that if we place our blueberry galaxy at $z > 0.1$, we may not be able to resolve its two components (i.e., a disk and inner Sérsic component) using SDSS-like data with a beam size of $1\farcs2$ FWHM (see Ross et al. 2011). Our experiment indicates that if a faint LSB old stellar disk in GPs at relatively higher redshifts is indeed very common, it can be detected only with very sensitive and high-angular-resolution observations performed using either bigger ground- or space-based telescopes.

The extreme emission-line nature of CELLs galaxies originates from their recent strong starburst event. The mechanism responsible for triggering such strong starburst events in these systems remains unexplored. In this context, the stellar and gas kinematics of our blueberry galaxy can shed some light on this aspect. Our blueberry galaxy has disturbed kinematics, showing a misalignment of $\sim 30°$ between the stellar and gaseous kinematic major axes. In general, such kinematic misalignment in galaxies indicates signs of galaxy interaction and merger or external gas accretion (Jaiswal & Omar 2013; van de Voort et al. 2015; Jin et al. 2016; Paswan et al. 2018; Li et al. 2021). Furthermore, the study by Lofthouse et al. (2017) has also shown evidence of a minor merger in their two GPs. Recently, Kanekar et al. (2021) presented the estimates of the H I gas mass in 40 GPs observed with the single radio dish Arecibo Telescope and Green Bank Telescope (GBT). Interestingly, they found that 9 of their 40 GPs lie above (>0.6 dex) the local M_{HI}–M_B relation (e.g., Dénes et al. 2014), suggesting that these 9 GPs are gas rich for their given optical luminosity and might be experiencing external gas accretion or minor merger. From our discussion above, it seems that an external gas accretion via galaxy interaction or minor merger might be one of the potential causes for triggering starburst

events in CELLs galaxies. Nevertheless, this scenario needs to explore further in greater depth using a large sample of CELLs galaxies.

It is important to point out here that a good fraction of CELLs galaxies have already been identified as LyC leakers and/or Lyα emitters (e.g., Izotov et al. 2016; Yang et al. 2017b; Verhamme et al. 2017; Izotov et al. 2018a, 2018b, 2021), mimicking their high-redshift counterparts that have contributed to the reionization process at $z \geqslant 6$. However, the host properties of these local counterparts show the presence of an old stellar population extending to a disk-like structure, unlike their high-redshift counterparts. The host properties of high-z galaxies are expected to be very young (maybe having their first-generation stars) and compact without an old stellar extended disk-like structure. It means that mechanisms that support the escape of ionizing photons from local CELLs galaxies may be different from those at play during the epoch of reionization. Along this line, the upcoming JWST would play a vital role in establishing the true underlying nature of the stellar population in high-redshift galaxies, at the same time establishing a possible connection with blueberries like SHOC 579 studied here.

Our main conclusions are:

1. The blueberry source studied here has recently ($\leqslant$10 Myr) formed over an underlying LSB disk of its host galaxy. To date, this blueberry galaxy is the most massive and metal-rich one for which we have direct observational evidence of an old stellar population.
2. Based on the modeling of stacked spectra showing a clear detection of the Mg I λ5173,5167 absorption line, we find the average mass-weighted age of the stellar population to be $\sim$5 Gyr and $\sim$7 Gyr for the blueberry component and the stellar disk, respectively. These estimates are consistent with our results from the best-fit SED model.
3. This work reveals the first kinematics of stars and gas of a blueberry galaxy based on locally stacked spectra from the MaNGA IFU observation. In it, the studied blueberry galaxy is found to be dispersion dominated in the ionized gas component and mildly rotation supported in the stellar component. Furthermore, these stellar and gaseous components are misaligned with each other.
4. The structural and SFH analyses of the host galaxy of our blueberry in this work and GPs presented by Amorín et al. (2012) and Clarke et al. (2021) in the literature suggest that CELLs galaxies (i.e., blueberries and GPs) do not represent peculiar cases of dwarf galaxy evolution. In fact, with respect to the structural properties of their host galaxies, they are compatible with a common evolutionary track of the main population of BCDs. In other words, the CELLs galaxies are luminous counterparts of local low-luminous BCDs. Their extreme emission-line properties are likely due to recent strong starburst events, potentially triggered by an external gas accretion process.
5. As such, CELLs galaxies are often referred to as the best analogs of sources at the epoch of reionization ($z > 6$). However, the above conclusion revealing the presence of old stars in CELLs galaxies would imply that mechanisms that allow the escape of ionizing photons in these local objects may be different from those at play during the epoch of reionization. Exploring the physical process that drives the escape of ionizing photons in both local and high-redshift LyC leakers is very important.

We thank the anonymous referee for constructive suggestions that have greatly improved the content and quality of the paper. A.P. thanks R. Amorin and P. Papaderos for kindly providing the data points used in Figure 7. A.P. also thanks Kuldeep Singh for his help in making Figure 11. This research has made use of the SAO/NASA Astrophysics Data System (ADS) operated by the Smithsonian Astrophysical Observatory (SAO) under a NASA grant.

Software: SExtractor (Bertin & Arnouts 1996), GALFIT (Peng et al. 2002), IRAF (Tody 1986), PHOTUTIL (Bradley et al. 2020), ASTROPY (Price-Whelan et al. 2018), PCIGALE (Boquien et al. 2019), DRP (Law et al. 2016), DAP (Westfall et al. 2019), pPXF (Cappellari & Emsellem 2004)

Appendix A
PSF-matched Photometry

The total magnitudes of the central blueberry region and the full galaxy are estimated using the aperture photometry technique. Because the images from the FUV to IR bands are taken from different survey/instruments whose PSFs are different from each other, we therefore applied a PSF-matching technique, before estimating the fluxes of the blueberry region and full galaxy. In this technique, we first estimated various PSF kernels between the GALEX FUV image (having the largest PSF among all the bands) and the rest of the other band images (i.e., from the optical to IR bands that have a better PSF compared to the FUV band) using the PHOTUTIL (Bradley et al. 2020) task available in the ASTROPY (Price-Whelan et al. 2018) package. We did not apply the PSF matching on the GALEX NUV band image as its PSF is very close to the FUV-band image. After obtaining various PSF kernels, we convolved them over their respective band images from optical to IR. This process provides us with all the band images from FUV to IR having a similar PSF. We then measured the aperture sizes of the central blueberry region only and the full galaxy in the SDSS i band, which are respectively found to be $\sim$2″ and 8″ in radius. In the rest of the band images, we used the same aperture sizes for the central blueberry region only and the full galaxy. Finally, we estimated the magnitudes of the galaxy in these two apertures separately using all the PSF-matched band images from FUV to IR. Note that in each case, the magnitude of the central blueberry region is estimated after subtracting background contamination from the surrounding LSB envelope, where the background contamination is measured using an annular region of 3 pixels around the central blueberry region.

Appendix B
SED Modeling

We constructed a multiband SED for the full galaxy and the central blueberry region separately using archival data from the FUV to IR bands. The fluxes for the SED construction are obtained from our PSF-matched photometry as explained in the preceding section. Some of the physical properties of the full galaxy and blueberry component have been derived by fitting the stellar population model with nebular lines using PCIGALE (Boquien et al. 2019). In that, we use the BC03 stellar population library (Bruzual & Charlot 2003) with exponentially declining star formation histories with late bursts having a Salpeter initial mass function (IMF; Salpeter 1955) with lower and upper mass cutoffs at 0.1 and 100 $M_{\odot}$, respectively. While performing the SED modeling, we have used an exponentially declining SFH with a late burst. The e-folding timescale of the

main stellar population is varied from $\tau_{\rm main} = 200$, 250, 300, 350, 400, 500, 600, 700, 1000, 1500, and 2000 Myr after some experimentation. The e-folding timescale of the late burst, $\tau_{\rm burst} = 20$, 30, 40, 50, 70, 100, and 200 Myr. Similarly, the age of the main stellar population has also been varied from 1000 to 9000 Myr, in steps of 200 Myr up to 2000 Myr and 500 Myr beyond 2000 Myr. Initially, we have varied metallicity values from 0.004, 0.008, and 0.02. The metallicity values for the best-fit models for the full galaxy and the blueberry region are found to be 0.02 and 0.008, respectively. These values are in accordance with our measurements from the MaNGA IFU data. The values of the color excess, $E(B-V)$, are used in the range of 0.1–0.2, guided by our measurements using the Balmer decrement from the MaNGA spectra. For the reduction factor for the old stellar population, we followed the Calzetti relation $E(B-V)_{\rm star} = 0.44 \times E(B-V)_{\rm nebular}$. We apply Calzetti extinction law (Calzetti et al. 2000) for dust modeling. The dust attenuation curve has a UV bump at 2175 Å with an amplitude of $\sim 1/3$ that of the Milky Way bump and the overall power-law slope of the curve is fixed at $n = -\delta + 0.75$, where δ is the slope deviation. In our modeling, we have varied δ from -0.5 to -0.1 in steps of 0.1. For the best-fit model ($\chi^2_{\rm reduced,full} = 8.0$ and $\chi^2_{\rm reduced,BBonly} = 5.2$) presented in Figure 4, $\delta = -0.25$ for the blueberry and -0.2 for the full-galaxy model. These slopes are similar to the slope of the SMC extinction curve (although slightly shallower), which may be more appropriate for high-redshift SFGs (Salim et al. 2018) and their local analogs. We obtain $\tau_{\rm main} = 250$ Myr, total stellar mass $M_* = 5.2 \times 10^9\ M_\odot$, and mass-weighted stellar age of 7.05 Gyr, while for the blueberry component, we obtain the stellar mass $M_* = 4.5 \times 10^8\ M_\odot$ with a mass-weighted age of the stellar population of 5.6 Gyr. The central blueberry component had $\tau_{\rm burst} = 100$ Myr and age of the starburst population $\rm burst_{age} = 10$ Myr. In addition to χ^2 as a goodness of fit, we also paid attention to comparing and picking the best SED models, which are able to explain the observation better. For example, we have compared the ratio of the rest-frame EW of strong emission lines such as EW(O[III])/EW(Hα). This ratio is 0.96 from the observed MaNGA spectra while this ratio is 1.1 from our best-fit SED model of the blueberry component. The mass-weighted stellar population age from our best-fit model matches closely that obtained from the pPXF modeling of the stacked spectra (see Appendix D below).

Appendix C
GALFIT Modeling

We discuss here the 2D modeling of our studied galaxy's light distribution in the SDSS i band using the GALFIT tool provided by Peng et al. (2002). For the GALFIT modeling of our galaxy, we compile the Gaussian PSF model obtained after creating a PSF kernel model image with 1.″06 FWHM. This PSF size for the SDSS i-band image is taken per the information provided in the SDSS Science Archive Server. With this, we first proceed with a simple two-component fitting—an inner Sérsic component surrounded by an exponentially declining disk. The first GALFIT run on the full galaxy using two components and without any constraints resulted in a significantly off-centered disk toward the southwest of the galaxy. Such a highly off-centered disk is unphysical. In a subsequent GALFIT run, we therefore constrained both components to have a common center. This approach, however, yielded an improper model, which is confirmed by an inspection of its residual image (i.e., observed minus model). To obtain the best-fit model to the full galaxy, we applied a different approach—we first model the underlying disk component and then the inner Sérsic component. Prior to fitting the exponential disk, we masked the bright inner component of the galaxy with a circular mask of $\sim 2''$ in radius as shown in Figure 6(b). This masking ensures that any effect due to the central bright region of the galaxy is minimized and also does not rule out the possible existence of an off-centered disk, if it indeed exists.

Table 1
The Best Output Parameters Obtained from the GALFIT Fitting to the Full Galaxy

Parameters	Sérsic Component	Exponential Component
Center (x, y)	(50.27 ± 0.06, 50.75 ± 0.07)	(46.63 ± 0.63, 51.68 ± 0.49)
Integrated magnitude (AB)	17.63 ± 0.03	17.65 ± 0.05
Scale length (kpc)	⋯	1.54 ± 0.13
Effective radius (pc)	217 ± 51	⋯
Sérsic index	1.48 ± 1.21	⋯
Axis ratio (b/a)	0.69 ± 0.21	0.66 ± 0.03
Position angle (deg)	64 ± 20	69 ± 5
Fourier amplitude	⋯	−0.57 ± 0.05
Fourier mode phase angle (deg)	⋯	−11 ± 12

Because our preliminary visual inspection of the galaxy shows the presence of a sheared disk-like light distribution around the central blueberry component—indicating a possible lopsided disk—we therefore modified the pure exponential disk function as given by Equation (C1) into Equation (C2), after including the first-order Fourier mode as follows:

$$I(x, y) = I_0 \exp\left(\frac{-r(x, y)}{r_h}\right) \tag{C1}$$

$$I(x, y) = I_0 \exp\left(\frac{-r(x, y) \times \left(1 + \sum_{m=1}^{N} a_m \cos\left(m(\theta + \phi_m)\right)\right)}{r_h}\right). \tag{C2}$$

In the above equations, I_0 and r_h are the peak intensity and scale length of the exponential disk, respectively, and $m = 1$ represents the first-order Fourier mode. $r(x, y)$ represents the radial coordinates of a standard ellipse, which is defined as

$$r(x, y) = \left(|x - x_0|^2 + \left|\frac{y - y_0}{q}\right|^2\right)^{\frac{1}{2}}. \tag{C3}$$

Here, q and a_m are the axis ratio and Fourier amplitude, respectively. $(\theta + \phi_m)$ represents the relative angle between mode m and the position angle (PA) of the standard ellipse (Peng et al. 2010), where the θ is defined as $\tan^{-1}((y - y_0)/(x - x_0)q)$. Using the model described above, we found a better fit to the underlying disk as confirmed by obtaining the best residual image. We then fit a simple Sérsic component to the obtained residual image (see Figure 6(d)). The complete model of our galaxy reveals that the centers of two components are indeed not common, indicating the presence of an off-centered disk. The final GALFIT model of the full galaxy and its residual are shown in Figures 6(c) and (f), respectively. We further analyzed the statistics of the residual image using the distribution of pixel

values within the dashed box as shown in Figure 6(f). This distribution follows a normal distribution function, whose μ and σ are found to be $\sim$0.0034 and $\sim$0.0542 nmgy, respectively. Finally, the GALFIT-modeled images and fitted parameters are presented in Figure 6 and Table 1, respectively.

Appendix D
Integrated Spectral Analyses

In our analysis, we noticed that the spectral features related to the underlying old stellar population such as the Balmer and Mg I λ5173 absorption lines are too faint to detect in a spatially resolved manner using the MaNGA datacube. We therefore performed the spectra stacking using a few hundred spectra from both the central blueberry component and surrounding faint LSB-disk regions. The stacked spectra from these two regions are shown in Figures 12(a) and (b), where red stellar continuum fittings are drawn using pPXF code with MILES stellar libraries (Cappellari & Emsellem 2004). These fittings clearly indicate the presence of underlying stellar absorption features and lead to the estimates of the mean stellar ages of $\sim$5 Gyr and $\sim$7.4 Gyr, respectively, for the blueberry component and faint LSB-disk regions.

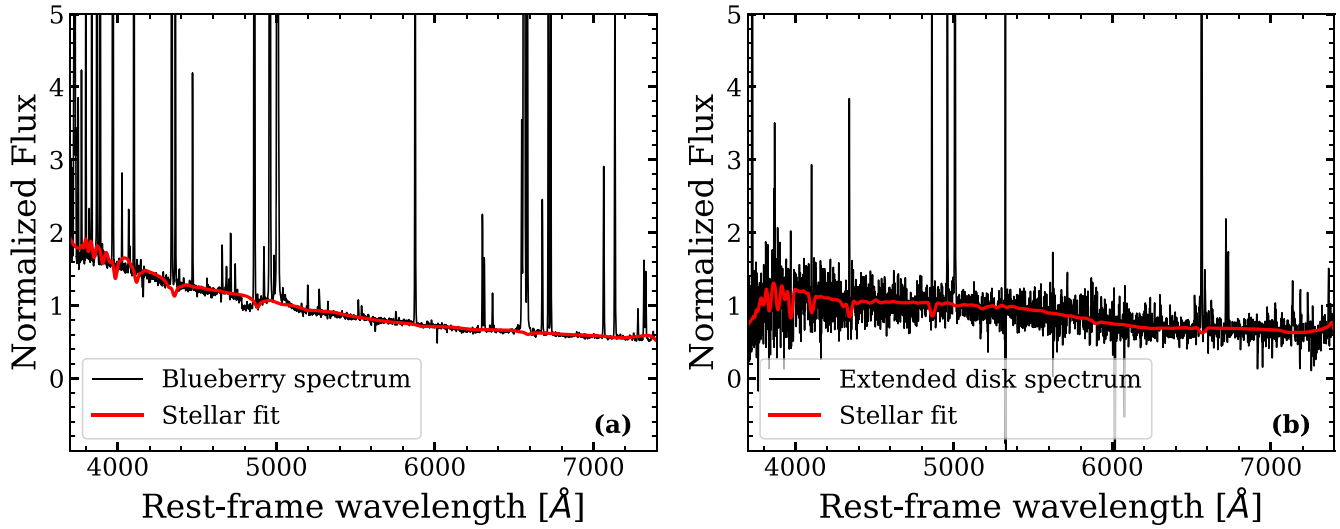

Figure 12. The stellar-model fit (red line) to the observed stacked spectra of (a) central blueberry region and (b) outer LSB stellar disk. These models are fitted using pPXF code with MILES stellar libraries. In each case, the observed spectra are shown by black lines.

ORCID iDs

Abhishek Paswan https://orcid.org/0000-0002-2657-9044
Kanak Saha https://orcid.org/0000-0002-8768-9298
Anshuman Borgohain https://orcid.org/0000-0002-2870-7716
Claus Leitherer https://orcid.org/0000-0003-2685-4488
Suraj Dhiwar https://orcid.org/0000-0001-8650-205X

References

Abazajian, K. N., Adelman-McCarthy, J. K., Agüeros, M. A., et al. 2009, ApJS, 182, 543
Adami, C., Scheidegger, R., Ulmer, M., et al. 2006, A&A, 459, 679
Agertz, O., Teyssier, R., & Moore, B. 2011, MNRAS, 410, 1391
Amorín, R., Pérez-Montero, E., Vílchez, J. M., & Papaderos, P. 2012, ApJ, 749, 185
Amorín, R. O., Pérez-Montero, E., & Vílchez, J. M. 2010, ApJL, 715, L128
Baldwin, J. A., Phillips, M. M., & Terlevich, R. 1981, PASP, 93, 5
Becker, A. C., Homrighausen, D., Connolly, A. J., et al. 2012, MNRAS, 425, 1341
Bertin, E., & Arnouts, S. 1996, A&AS, 117, 393
Bian, F., Fan, X., McGreer, I., Cai, Z., & Jiang, L. 2017, ApJL, 837, L12
Blanton, M. R., Bershady, M. A., Abolfathi, B., et al. 2017, AJ, 154, 28
Boquien, M., Burgarella, D., Roehlly, Y., et al. 2019, A&A, 622, A103
Bradley, L., Sipőcz, B., Robitaille, T., et al. 2020, astropy/photutils: v1.0.0, Zenodo, doi:10.5281/zenodo.4044744
Brown, W. R., Geller, M. J., Fabricant, D. G., & Kurtz, M. J. 2001, AJ, 122, 714
Bruzual, G., & Charlot, S. 2003, MNRAS, 344, 1000
Bundy, K., Bershady, M. A., Law, D. R., et al. 2015, ApJ, 798, 7
Cairós, L. M., Vílchez, J. M., González Pérez, J. N., Iglesias-Páramo, J., & Caon, N. 2001, ApJS, 133, 321
Calzetti, D., Armus, L., Bohlin, R. C., et al. 2000, ApJ, 533, 682
Cappellari, M., & Emsellem, E. 2004, PASP, 116, 138
Cardamone, C., Schawinski, K., Sarzi, M., et al. 2009, MNRAS, 399, 1191
Clarke, L., Scarlata, C., Mehta, V., et al. 2021, ApJL, 912, L22
Dale, D. A., Cohen, S. A., Johnson, L. C., et al. 2009, ApJ, 703, 517
Dénes, H., Kilborn, V. A., & Koribalski, B. S. 2014, MNRAS, 444, 667
D'Onghia, E., Burkert, A., Murante, G., & Khochfar, S. 2006, MNRAS, 372, 1525
Dutton, A. A. 2009, MNRAS, 396, 121
Ferrara, A., & Tolstoy, E. 2000, MNRAS, 313, 291
Finkelstein, S. L., Hill, G. J., Gebhardt, K., et al. 2011, ApJ, 729, 140
Fletcher, T. J., Tang, M., Robertson, B. E., et al. 2019, ApJ, 878, 87
Genel, S., Fall, S. M., Hernquist, L., et al. 2015, ApJL, 804, L40
Gil de Paz, A., & Madore, B. F. 2005, ApJS, 156, 345
Gunn, J. E., Carr, M., Rockosi, C., et al. 1998, AJ, 116, 3040
Gunn, J. E., Siegmund, W. A., Mannery, E. J., et al. 2006, AJ, 131, 2332
Guseva, N. G., Papaderos, P., Izotov, Y. I., Noeske, K. G., & Fricke, K. J. 2004, A&A, 421, 519
Guseva, N. G., Papaderos, P., Meyer, H. T., Izotov, Y. I., & Fricke, K. J. 2009, A&A, 505, 63
Henry, A., Scarlata, C., Martin, C. L., & Erb, D. 2015, ApJ, 809, 19
Hoyos, C., Koo, D. C., Phillips, A. C., Willmer, C. N. A., & Guhathakurta, P. 2005, ApJL, 635, L21
Hubble, E., & Tolman, R. C. 1935, ApJ, 82, 302
Izotov, Y. I., Guseva, N. G., Fricke, K. J., et al. 2021, A&A, 646, A138
Izotov, Y. I., Guseva, N. G., & Thuan, T. X. 2011, ApJ, 728, 161
Izotov, Y. I., Lipovetsky, V. A., Chaffee, F. H., et al. 1997, ApJ, 476, 698
Izotov, Y. I., Schaerer, D., Thuan, T. X., et al. 2016, MNRAS, 461, 3683
Izotov, Y. I., Schaerer, D., Worseck, G., et al. 2018a, MNRAS, 474, 4514
Izotov, Y. I., Worseck, G., Schaerer, D., et al. 2018b, MNRAS, 478, 4851
Jaiswal, S., & Omar, A. 2013, JApA, 34, 247
Jaskot, A. E., Dowd, T., Oey, M. S., Scarlata, C., & McKinney, J. 2019, ApJ, 885, 96
Jaskot, A. E., & Oey, M. S. 2014, ApJL, 791, L19
Jin, Y., Chen, Y., Shi, Y., et al. 2016, MNRAS, 463, 913
Kakazu, Y., Cowie, L. L., & Hu, E. M. 2007, ApJ, 668, 853
Kanekar, N., Ghosh, T., Rhoads, J., et al. 2021, ApJL, 913, L15
Kassin, S. A., Weiner, B. J., Faber, S. M., et al. 2012, ApJ, 758, 106
Kauffmann, G., Heckman, T. M., White, S. D. M., et al. 2003, MNRAS, 341, 33
Kennicutt, R. C., J. 1998, ApJ, 498, 541
Kim, K. J., Malhotra, S., Rhoads, J. E., & Yang, H. 2021, ApJ, 914, 2
Kimm, T., Katz, H., Haehnelt, M., et al. 2017, MNRAS, 466, 4826
Krueger, H., Fritze-v. Alvensleben, U., & Loose, H. H. 1995, A&A, 303, 41
Kunth, D., Maurogordato, S., & Vigroux, L. 1988, A&A, 204, 10
Kunth, D., & Sargent, W. L. W. 1981, A&A, 101, L5
Kunth, D., & Schild, H. 1986, A&A, 169, 71
Law, D. R., Cherinka, B., Yan, R., et al. 2016, AJ, 152, 83
Li, S.-l., Shi, Y., Bizyaev, D., et al. 2021, MNRAS, 501, 14
Lian, J. H., Kong, X., Jiang, N., Yan, W., & Gao, Y. L. 2015, MNRAS, 451, 1130
Lintott, C., Schawinski, K., Bamford, S., et al. 2011, MNRAS, 410, 166
Lintott, C. J., Schawinski, K., Slosar, A., et al. 2008, MNRAS, 389, 1179
Lofthouse, E. K., Houghton, R. C. W., & Kaviraj, S. 2017, MNRAS, 471, 2311
Malkan, M. A., & Malkan, B. K. 2021, ApJ, 909, 92
Martin, D. C., Fanson, J., Schiminovich, D., et al. 2005, ApJL, 619, L1
Meynet, G., & Maeder, A. 2005, A&A, 429, 581
Mo, H. J., Mao, S., & White, S. D. M. 1998, MNRAS, 295, 319
Nakajima, K., & Ouchi, M. 2014, MNRAS, 442, 900
Newman, S. F., Genzel, R., Förster Schreiber, N. M., et al. 2013, ApJ, 767, 104
Noeske, K. G., Papaderos, P., Cairós, L. M., & Fricke, K. J. 2003, A&A, 410, 481
O'Donnell, J. E. 1994, ApJ, 422, 158
Oke, J. B. 1974, ApJS, 27, 21
Osterbrock, D. E., & Bochkarev, N. G. 1989, SvA, 33, 694
Östlin, G., Amram, P., Bergvall, N., et al. 2001, A&A, 374, 800
Pahwa, I., & Saha, K. 2018, MNRAS, 478, 4657
Papaderos, P., Guseva, N. G., Izotov, Y. I., & Fricke, K. J. 2008, A&A, 491, 113
Papaderos, P., Izotov, Y. I., Fricke, K. J., Thuan, T. X., & Guseva, N. G. 1998, A&A, 338, 43
Papaderos, P., Izotov, Y. I., Thuan, T. X., et al. 2002, A&A, 393, 461
Papaderos, P., Loose, H. H., Fricke, K. J., & Thuan, T. X. 1996a, A&A, 314, 59
Papaderos, P., Loose, H. H., Thuan, T. X., & Fricke, K. J. 1996b, A&AS, 120, 207
Paswan, A., Omar, A., & Jaiswal, S. 2018, MNRAS, 473, 4566
Paswan, A., Omar, A., & Jaiswal, S. 2019, MNRAS, 482, 3803
Paswan, A., Saha, K., & Dhiwar, S. 2021, arXiv:2102.08240
Paswan, A., Saha, K., Leitherer, C., & Schaerer, D. 2022, ApJ, 924, 47
Peng, C. Y., Ho, L. C., Impey, C. D., & Rix, H.-W. 2002, AJ, 124, 266
Peng, C. Y., Ho, L. C., Impey, C. D., & Rix, H.-W. 2010, AJ, 139, 2097
Pérez-Montero, E., Contini, T., Lamareille, F., et al. 2009, A&A, 495, 73
Pettini, M., & Pagel, B. E. J. 2004, MNRAS, 348, L59
Pettini, M., Shapley, A. E., Steidel, C. C., et al. 2001, ApJ, 554, 981
Price-Whelan, A. M., Sipőcz, B., Günther, H., et al. 2018, AJ, 156, 123
Rathaus, B., & Sternberg, A. 2016, MNRAS, 458, 3168
Reverte, D., Vílchez, J. M., Hernández-Fernández, J. D., & Iglesias-Páramo, J. 2007, AJ, 133, 705
Rong, Y., Yang, H., Zhang, H.-x., et al. 2018, arXiv:1806.10149
Ross, A. J., Ho, S., Cuesta, A. J., et al. 2011, MNRAS, 417, 1350
Saha, K., Tandon, S. N., Simmonds, C., et al. 2020, NatAs, 4, 1185
Sales, L. V., Navarro, J. F., Schaye, J., et al. 2009, MNRAS, 399, L64
Salim, S., Boquien, M., & Lee, J. C. 2018, ApJ, 859, 11
Salpeter, E. E. 1955, ApJ, 121, 161
Salzer, J. J., Williams, A. L., & Gronwall, C. 2009, ApJL, 695, L67
Scannapieco, C., Tissera, P. B., White, S. D. M., & Springel, V. 2008, MNRAS, 389, 1137
Schombert, J. M., McGaugh, S. S., & Eder, J. A. 2001, AJ, 121, 2420
Schombert, J. M., Pildis, R. A., Eder, J. A., & Oemler, Augustus, J. 1995, AJ, 110, 2067
Sersic, J. L. 1968, Atlas de Galaxias Australes (Córdoba: Observatorio Astronomico)
Shapley, A. E., Steidel, C. C., Strom, A. L., et al. 2016, ApJL, 826, L24
Smee, S. A., Gunn, J. E., Uomoto, A., et al. 2013, AJ, 146, 32
Sung, E.-C., Han, C., Ryden, B. S., Chun, M.-S., & Kim, H.-I. 1998, ApJ, 499, 140
Terlevich, R., Melnick, J., Masegosa, J., Moles, M., & Copetti, M. V. F. 1991, A&AS, 91, 285
Thornley, M. D., Förster Schreiber, N. M., Lutz, D., et al. 2000, ApJ, 539, 641
Thuan, T. X., Alimi, J.-M., Gott, J., Richard, I., & Schneider, S. E. 1991, ApJ, 370, 25
Tody, D. 1986, Proc. SPIE, 627, 733
Tolman, R. C. 1930, PNAS, 16, 511
Tolman, R. C. 1934, PNAS, 20, 169
Trebitsch, M., Blaizot, J., Rosdahl, J., Devriendt, J., & Slyz, A. 2017, MNRAS, 470, 224
Trebitsch, M., Volonteri, M., & Dubois, Y. 2020, MNRAS, 494, 3453

Übler, H., Naab, T., Oser, L., et al. 2014, MNRAS, 443, 2092
van de Voort, F., Davis, T. A., Kereš, D., et al. 2015, MNRAS, 451, 3269
Van Rossum, G., & Drake, F. L. 2009, Python 3 Reference Manual (Scotts Valley, CA: CreateSpace)
van Zee, L. 2001, AJ, 121, 2003
Vanzella, E., Nonino, M., Cupani, G., et al. 2018, MNRAS, 476, L15
Verhamme, A., Orlitová, I., Schaerer, D., et al. 2017, A&A, 597, A13
Wake, D. A., Bundy, K., Diamond-Stanic, A. M., et al. 2017, AJ, 154, 86
Wang, B., Heckman, T. M., Leitherer, C., et al. 2019, ApJ, 885, 57
Westfall, K. B., Cappellari, M., Bershady, M. A., et al. 2019, AJ, 158, 231
Yang, H., Malhotra, S., Gronke, M., et al. 2016, ApJ, 820, 130
Yang, H., Malhotra, S., Gronke, M., et al. 2017b, ApJ, 844, 171
Yang, H., Malhotra, S., Rhoads, J. E., & Wang, J. 2017a, ApJ, 847, 38
York, D. G., Adelman, J., Anderson, John E., J., et al. 2000, AJ, 120, 1579